



Morphometric analysis of the North Liuleng Shan Fault in the northern Shanxi Graben System, China: Insights into active deformation pattern and fault evolution

Quanxing Luo^{a,b,c}, Lindsay Schoenbohm^c, Jeremy Rimando^d, Youli Li^b, Chuanyou Li^a,
Jianguo Xiong^{a,*}

^a State Key Laboratory of Earthquake Dynamics, Institute of Geology, China Earthquake Administration, Beijing, China

^b Key Laboratory of Earth Surface Processes of Ministry of Education, Peking University, Beijing, China

^c Department of Chemical and Physical Sciences, University of Toronto Mississauga, Mississauga, Ontario, Canada

^d School of Earth, Environment and Society, McMaster University, Hamilton, Ontario, Canada

ARTICLE INFO

Keywords:

Geomorphic indices
Shanxi Graben System
North Liuleng Shan Fault
Active deformation
North China

ABSTRACT

The North Liuleng Shan Fault (NLSF) is one of the major active faults in the northern Shanxi Graben System (SGS) in North China. Although the fault has been investigated extensively in terms of late Quaternary activity, its active deformation pattern is still poorly characterized. In this study, we conducted a morphometric analysis of the fault using various geomorphic indices to assess the along-strike relative uplift rates, which include basin relief, slope, mountain front sinuosity (S_{mf}), hypsometric integral (HI) and curves, valley floor width-to-height ratio (V_f), asymmetry factor (A_f), basin elongation ratio (R_e), and normalized channel steepness indices (k_{sn}). Our findings indicate that the central portion of the fault has experienced higher relative uplift rates than the southwestern and northeastern portions, as demonstrated by higher basin-averaged slopes and k_{sn} values, and lower V_f , R_e , and S_{mf} values. This spatial distribution pattern of relative uplift rates appears to correlate well with along-strike changes in the fault geometry and kinematics of the NLSF. We interpret the EW-striking, central portion of the NLSF as a releasing bend formed by the NE-striking, right-stepping, en-echelon southwestern and northeastern portions of the fault system, which are characterized by right-lateral oblique slip. Furthermore, the northeastward increase in HI values along with the regional basin evolution history suggest that the NLSF likely propagated from southwest to northeast. We propose that the southwestern portion of the fault most probably initiated earlier and that the central and northeastern portions formed later as extensional structures at the termini of the fault zone. Our findings contribute to a better understanding of the tectonics and genesis of the basin-and-range geomorphology in the northern SGS.

1. Introduction

The Shanxi Graben System (SGS) is an important seismogenic zone in central North China that constitutes a collection of en-echelon-arranged basins (Fig. 1a; Xu and Ma, 1992; Xu et al., 1993). The dynamic mechanism, evolution history, and active tectonics of the SGS have long been of great interest to geologists (e.g., Xu and Ma, 1992; Xu et al., 1993; Li et al., 1998; Zhang et al., 1998a; Lv et al., 2014; Shi et al., 2015; Clinkscales et al., 2020, 2021; Luo et al., 2021, 2022b, 2023). The North Liuleng Shan Fault (NLSF), one of the major active faults in the northern domain of the SGS, is approximately 150 km long and exhibits an ENE-

striking Z-shaped trace along the northern piedmont of the Liuleng Shan ("Shan" means "mountains" in Chinese; Fig. 1b). The 1989 Datong-Yanggao earthquake swarm, which produced a M_s 6.1 mainshock (the largest earthquake in the SGS in the last 200 years) that resulted in a large number of fatalities and injuries and caused extensive property damage, struck the central portion of the Liuleng Shan piedmont (Fig. 1b; Zhuo et al., 2019). Since then, generations of geologists have conducted research on the deformation characteristics and paleo-earthquake history of the NLSF (Deng et al., 1994; Duan and Fang, 1995; Xu et al., 1996a, 2002; Yin et al., 1997; Sun, 2018; Sun et al., 2023; Luo et al., 2022a, 2022b). However, the longer-term active deformation

* Corresponding author.

E-mail address: xiongjg@pku.edu.cn (J. Xiong).

<https://doi.org/10.1016/j.geomorph.2023.108862>

Received 18 April 2023; Received in revised form 19 July 2023; Accepted 5 August 2023

Available online 11 August 2023

0169-555X/© 2023 Published by Elsevier B.V.

pattern of the NLSF remains poorly constrained, which limits our understanding of the geomorphological evolution along the fault and the mechanism responsible for strong earthquakes in the region.

The analysis of geomorphic indices has proven useful in addressing active tectonic issues, such as the identification of active structures and assessment of relative tectonic activity of faults or their segments in different tectonic settings worldwide (Wobus et al., 2003; Molin et al., 2004; Thompson Jobe et al., 2020; Rimando and Schoenbohm, 2020; Shi et al., 2020b; Krystopowicz et al., 2019; Bucci and Schoenbohm, 2022; Gusti et al., 2023). Several authors have attempted to investigate the tectonic geomorphology of the NLSF using geomorphic indices (Cheng and Yang, 1999; Yan et al., 2011). For example, Cheng and Yang (1999) conducted a joint analysis of geomorphic indices (e.g., mountain front sinuosity, valley width-depth relief ratio, and stream-gradient index measured from 1:10,000 scale topographic maps) and mountain front geomorphic features (e.g., fault scarp heights). The authors concluded that the NLSF can be divided into two segments (SW and NE segments) by the fault overlap zone in the vicinity of Dawang village (Fig. 1b), and with the NE segment being more strongly regulated by faulting than the SW segment. In addition, by calculating geomorphic indices like stream length-gradient, hypsometric integral, and basin shape index, Yan et al. (2011) analyzed five gullies locally concentrated in the central of the NLSF and found that the evolution of these gullies is closely tied to the NLSF. However, given the successful application of some emerging geomorphic indices (such as normalized channel steepness index: k_{sn} , discussed in more detail in the following section) and the new cognition of fault kinematics of the NLSF (Luo et al., 2022a, 2022b), a thorough

examination of the morphometric features along the mountain front may yield novel insights into the tectonic deformation pattern of the fault system.

In this study, we first use a combination of mountain front- and drainage basin-based geomorphic indices to examine the spatial distribution pattern of long-term relative uplift rates along the strike of the NLSF. Then, utilizing field observations and interpretations of high-resolution topographic data produced by the unmanned aerial vehicle (UAV) images-based structure from motion (SfM) technique, we present additional geomorphic evidence on the kinematics of the NLSF. Based on these data, we examine the active deformation pattern and discuss the possible evolutionary history of the NLSF. Our results contribute to the current knowledge of regional tectonics and geomorphology of the northern SGS.

2. Geological background

2.1. Tectonic setting

The Shanxi Graben System (SGS) is a Cenozoic intracontinental rift system (>2000 km away from the nearest active plate boundary) in North China, located between the North China Block to the east and the Ordos Block to the west (Fig. 1a; Clinkscales et al., 2021). The SGS has hosted >19 $M_s \geq 6$ earthquakes since 231 CE, including the M_s 8.0 Hongdong earthquake in 1303 CE (Xu et al., 1993). The sigmoid-shaped SGS consists of a series of grabens and half-grabens arranged in a left-stepping, en-echelon pattern, with a length of 1200 km and a width of

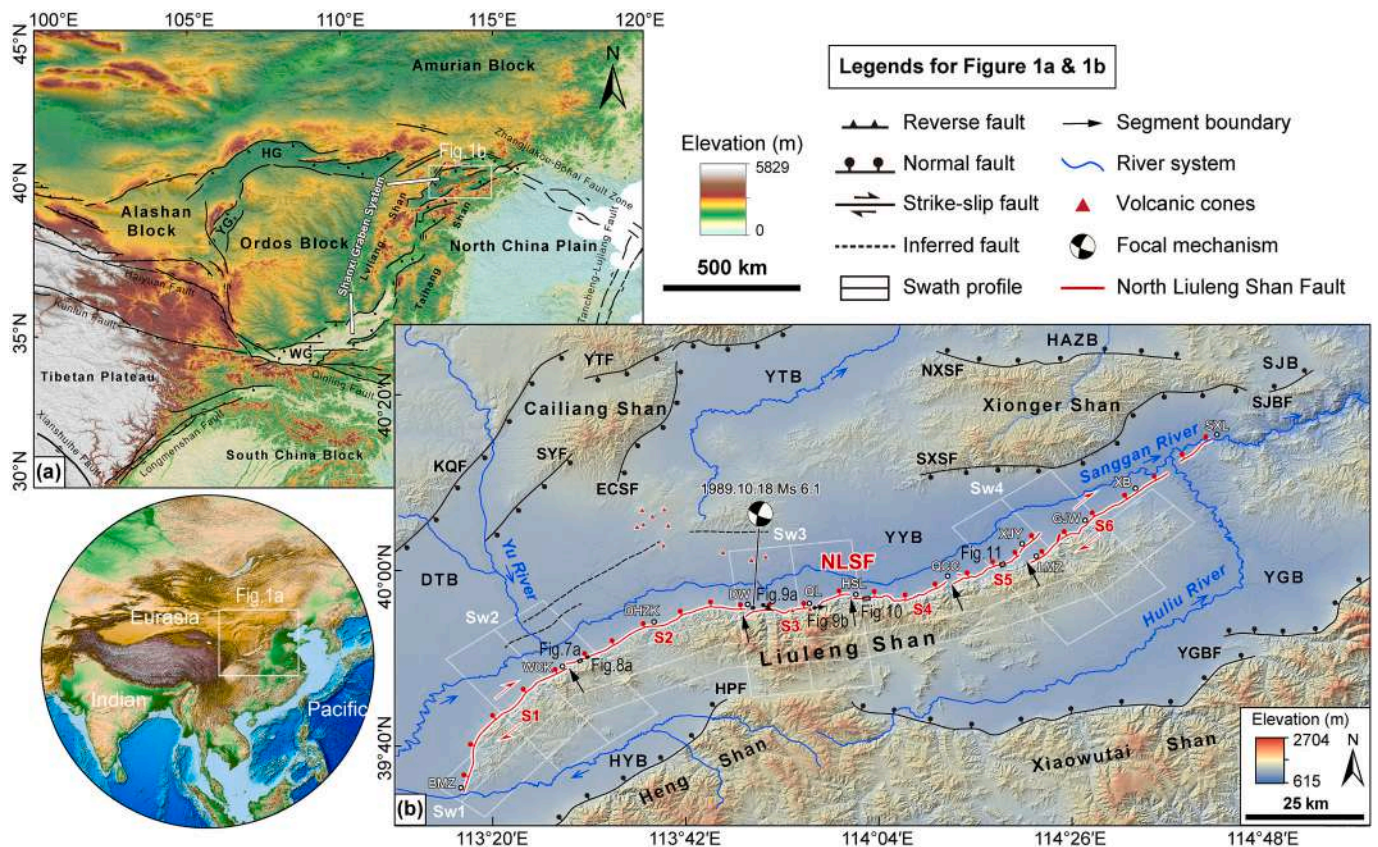


Fig. 1. Regional tectonics of the Shanxi Graben System and the North Liuleng Shan Fault. (a) Topographic map showing tectonic blocks and active faults in central China. Abbreviations: HG – Hetao Graben, YG – Yinchuan Graben, WG- Weihe Graben. (b) Topographic map showing active faults, Quaternary volcanoes, river systems, and basins around the Datong-Yanggao Basin. Abbreviations: YTB- Yanggao-Tianzhen Basin, HAZB- Huaianzhen Basin, SJB- Shenjing Basin, YYB- Yuguang Basin, DTB- Datong Basin, HYB- Hunyuan Basin, YGB- Yuguang Basin; YTF- Yanggao-Tianzhen Fault, KQF-Kouquan Fault, SYF- Shuiyu Fault, ECSF-East Cailiang Shan Fault, NXSF- North Xionger Shan Fault, SXSF- South Xionger Shan Fault, SJB- Shenjing Basin Fault, NLSF- North Liuleng Shan Fault, HPF- Hengshan Piedmont Fault, YGBF- Yuguang Basin Fault; BMZ-Beimazhuang, WCK- Wengchengkou, DHZK-Donghouzikou, DW- Dawang, QL-Qiulin, HSL-Huoshiling, QCC-Quchangcheng, XJY-Xiejiaoyao, LMZ-Longmazhuang, GJW-Gongjiawan, XB-Xinbu, SXL-Shixiali.

60–200 km (Xu and Ma, 1992; Xu et al., 1993; Li et al., 1998). The SGS can be divided into three domains according to the geometry and kinematics of the boundary faults: a central NNE-striking dextral trans-tensional segment and two ENE-striking extensional domains to the north and the south (Xu and Ma, 1992; Xu et al., 1993). Global Positioning System (GPS) observation data indicate that the right-lateral slip rate of the SGS is 1.4 ± 0.1 mm/yr, with little extensional deformation

(Hao et al., 2021; Wang and Shen, 2020). Earlier studies showed that, on the basis of Mesozoic fold-thrust structures, the central SGS was first initiated in the early Pliocene owing to the stress field induced by the interaction of the Indian, Eurasian, and Pacific plates (Xu and Ma, 1992; Xu et al., 1993). The extensional northern and southern domains formed as a consequence of the dextral shearing of the central segment (Xu and Ma, 1992). In contrast, recent low-temperature thermochronology and

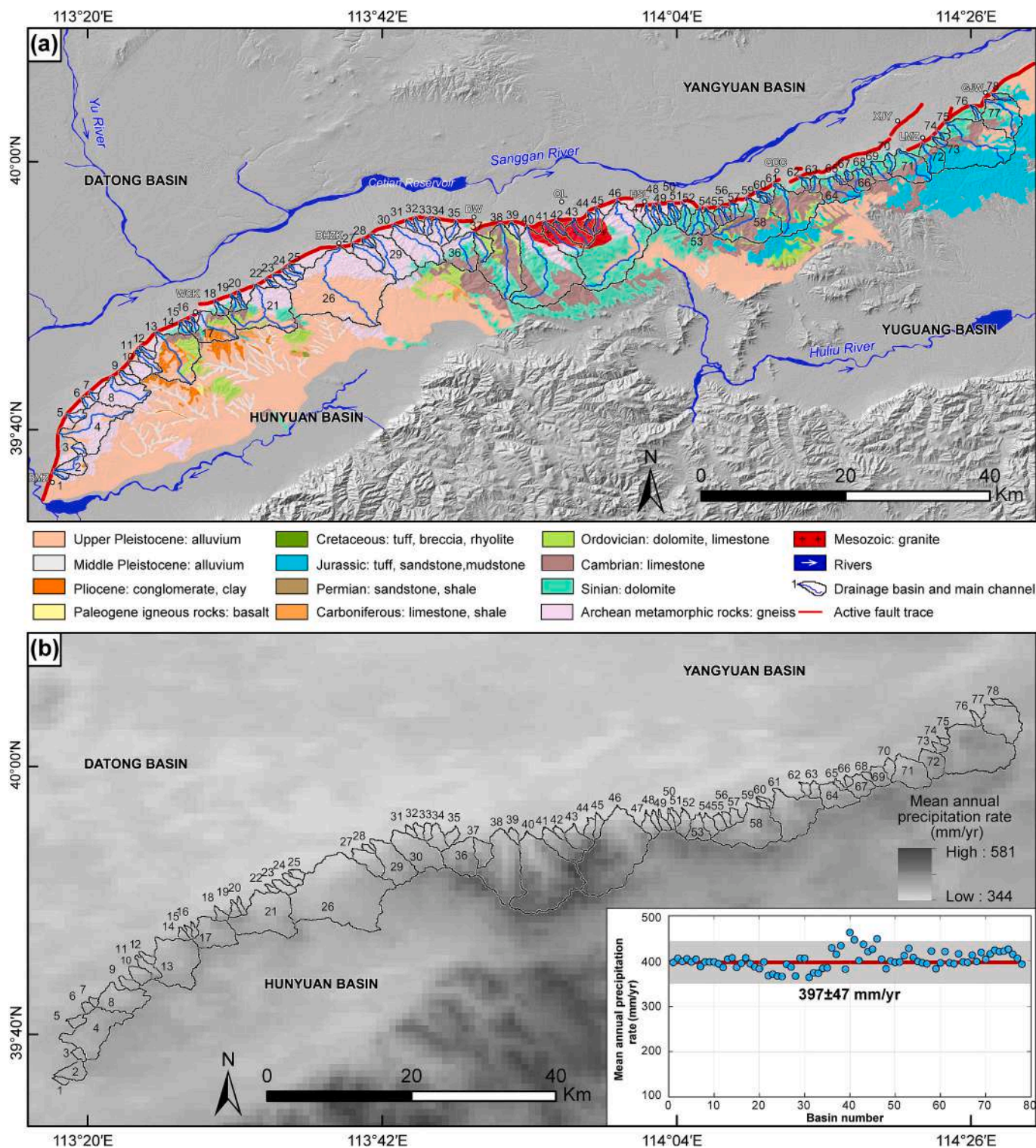


Fig. 2. Geological and precipitation maps of the Liuleng Shan. (a) A generalized geological map of the Liuleng Shan illustrating the substrate lithology of drainage basins referred to a 1:200,000 geological database (Li et al., 2017). (b) Mean annual precipitation in the Liuleng Shan area. Precipitation data are ~ 1 km² resolution from 1970 to 2000. The scatter plot shows the basin-averaged annual precipitation.

magnetostratigraphy argue for an earlier initiation of the SGS in the late Miocene (~7–10 Ma) (Su et al., 2021; Clinkscates et al., 2020, 2021; Bi et al., 2022).

This study focuses on a region in the northern SGS (Fig. 1a). Neotectonic studies have shown that the northern SGS is extending NNW-SSE at a rate of 1–2 mm/yr (Zhang et al., 1998a; Shi et al., 2015; Middleton et al., 2017; Zhao et al., 2017). Unlike the south and central SGS, which have been amagmatic during the Cenozoic, Eocene-Quaternary basalts erupted in the northern SGS (e.g., the Datong volcano groups; Xu and Ma, 1992; Clinkscates et al., 2021). Geophysical surveys reveal a low-velocity anomaly (or conductor) beneath the Datong volcanic area that extends from the upper mantle to the mid-crust (Zhang et al., 2016; Dou et al., 2021). Ai et al. (2019) proposed that rifting in the northern SGS is due to the combined effects of asthenospheric upwelling and counterclockwise rotation of the Ordos Block, while the rifting in the south could be a consequence of the uplift of the Tibetan Plateau. Although the northern SGS is seismically active, earthquake magnitudes are generally moderate (no more than M_s 7.0) according to both historical and instrumental records (Xu and Ma, 1992). It has also been shown that large earthquakes in the northern SGS are generally located in resistive zones above high conductivity anomalies (Zhang et al., 2016).

2.2. Geological and geomorphological setting

The northern SGS is a typical basin-and-range province, consisting of NE-SW-striking basins and parallel bedrock ranges (Fig. 1b; Xu and Ma, 1992; Xu et al., 1993, 2002; Li et al., 1998). The largest basin in the northern SGS is the Datong Basin, which is bounded by the Kouquan Fault to its west, the western segment of the NLSF to its east, and the Hengshan Piedmont Fault to its south (Fig. 1b). Sedimentation in the Datong Basin commenced in the Miocene (no later than 7 Ma; Bi et al., 2022) and sediment thickness reaches 1500 m adjacent to the Kouquan Fault (Xu and Ma, 1992). The Datong Basin is connected to the Yangyuan Basin to the east, and the Sangan River flows west to east through these two basins. The Huli River links the Datong-Yangyuan Basin to the Yuguang Basin in the southeast. These basins are also collectively referred to as the Nihewan Basin, which is famous for housing numerous Paleolithic sites and mammalian faunas (Zhu et al., 2001, 2004). Unlike the Yanggao-Tianzhen Basin, Yuguang Basin, and other half-grabens in the northern SGS, the Yangyuan Basin is a graben, defined by the NW-dipping NLSF in the south and the SE-dipping South Xionger Shan Fault in the north, with a basin floor elevation of 850–1200 m. The Yangyuan Basin is filled with Pliocene to Holocene lacustrine, fluvial, and wind-blown deposits (Xu et al., 2002). The fluvial-lacustrine sedimentary sequences named the Nihewan Beds (Barbour, 1924) date from the Late Pliocene to late Pleistocene according to magnetostratigraphic investigations (Deng et al., 2008; Liu et al., 2018). On the south side of the Yangyuan basin, the highlands of the Liuleng Shan are over 1100 m high, with the highest peak reaching 2420 m (Duan and Fang, 1995). The bedrock lithology of the Liuleng Shan varies along its strike (Fig. 2a). The southwestern part is primarily composed of Archean metamorphic rocks, the northeastern part is mainly made up of carbonate rocks of Proterozoic and Early Paleozoic age, and the central main peak of the Liuleng Shan is a Mesozoic granite intrusion. A global precipitation dataset indicates that the mean annual precipitation in the Liuleng Shan areas is 300–500 mm/yr (Fig. 2b; <http://www.worldclim.org/version2>).

2.3. North Liuleng Shan Fault

The NLSF, which defines the southern boundary of the Datong-Yangyuan Basin, extends northeastward from Beimazhuang village to Shixiali village (Fig. 1b). It separates the uplifted bedrock range of Liuleng Shan in the footwall from the downthrown Datong-Yangyuan Basin in the hanging wall. The fault is NE-striking in the southwest

and turns E-W-striking in the central section and then back to NE-striking in the northeast. The NLSF can be divided into six structural segments based on along-strike changes in fault geometry, such as 1–4 km-wide fault steps and fault overlap zones (Fig. 1b; Xu et al., 1996a, 2002). The central portion of the NLSF displaces an Early to Middle Pleistocene basaltic volcanic cone in the vicinity of Qiulin village, forming fault scarps with heights of 30–50 m, indicating the long-term activity of the fault (Deng et al., 1994; Xu et al., 1996a; Shi et al., 2020a). Trench investigations indicate that the NLSF has been active in the Holocene (Yin et al., 1997; Xu et al., 2002; Sun et al., 2023) and poses a high seismic hazard (Xu et al., 2017).

Previous studies proposed that the NLSF is a normal fault (Deng et al., 1994; Duan and Fang, 1995; Xu et al., 1996a, 2002; Cheng and Yang, 1999; Sun, 2018), except for the NE-striking southwesternmost segment, which was believed to behave as a right-lateral oblique-slip fault (Deng and Xu, 1995; Xu et al., 1996b). Our earlier work based on field investigation and interpretation of high-precision topographic data reveals that the southwesternmost segment of the NLSF is dominated by dextral strike-slip, with a strike-slip rate of 1.6 mm/yr and normal slip rate of ~0.1–0.2 mm/yr (Luo et al., 2022a). However, the evidence supporting the lateral movement of the fault is only based on offset stream channels. In this study, we provide new geomorphic evidence (e.g., offset terrace risers) within a more complete along-strike coverage to demonstrate that the NE-striking southwestern segment of the NLSF is characterized by right-lateral oblique-slip faulting. Additionally, our previous work concluded that the NE-striking northeastern segment of the NLSF is also characterized by a right-lateral oblique slip (Luo et al., 2022b), with right-lateral strike-slip and vertical slip rates both 0.2–0.3 mm/yr.

3. Methodology

This work takes a two-pronged approach. First, we use publicly accessible digital elevation model (DEM) data for topographic analysis and calculation of geomorphic indices. Second, we use high-precision topographic data obtained by UAV photogrammetry for the measurement of fault-related geomorphic features. Based on this study and other published data, our goal is to characterize the fault deformation pattern, investigate the connection between footwall block topography and along-strike variations in fault kinematics, and make inferences regarding the fault's tectonic evolutionary history.

3.1. Geomorphic analysis

The calculation of geomorphic indices and other topographic characterization in this study were all based on the MERIT DEM with a resolution of 90 m (http://hydro.iis.u-tokyo.ac.jp/~yamada/MERIT_DEM/). The MERIT DEM was developed by removing multiple error components (absolute bias, stripe noise, speckle noise, and tree height bias) from existing spaceborne DEMs (NASA SRTM3 v2.1, JAXA AW3D-30 m v1, and Viewfinder Panoramas' DEM). The quality of MERIT DEM data has been well assessed and it has been shown that MERIT DEM is highly reliable for areas with variable topography and land cover conditions, including the Earth's most rugged areas such as the High Mountain Asia (Liu et al., 2019; Uemaa et al., 2020).

Using the Hydrology toolset in ArcGIS, we extracted a total of 78 drainage basins along the mountain front covering the whole bedrock range of Liuleng Shan (No.1–78 from west to east; Fig. 2). These basins were confirmed on Google Earth satellite images to eliminate any basins that were caused by errors in the DEM. The size of basins varies from 0.89 km² (No.15) to 77.27 km² (No.26), which ensures that basins that are dominated by non-fluvial processes were excluded from our analysis, as the thresholds between colluvial and fluvial processes (the critical drainage area) are typically between 0.1 and 1 km² (Mitchell and Yanites, 2019). As described in more detail in the following sections, we calculated the relief, basin-averaged slope, hypsometric integral (HI)

values and curves, valley-floor-width-to-height ratio (V_f), asymmetry factor (A_f), elongation ratio (R_e), and normalized channel steepness index (k_{sn}) for those basins (Table S1). These calculated parameters are independent of drainage basin area (Fig. S1). In addition to these drainage basin-based parameters, we also measured the mountain front sinuosity (S_{mf}). These geomorphic indices might be direct (e.g., V_f , S_{mf} , and k_{sn}) or indirect (e.g., HI , A_f , and R_e) indications of relative uplift rates, and therefore have been used extensively for assessment of

relative uplift rates in different tectonic settings worldwide (Pérez-Peña et al., 2010; Ntokos et al., 2016; Saber et al., 2018; Rimando and Schoenbohm, 2020; Krystopowicz et al., 2019). We also constructed transverse and longitudinal topographic swath profiles along the mountain front to make inferences regarding the broad long-term distribution of vertical displacement.

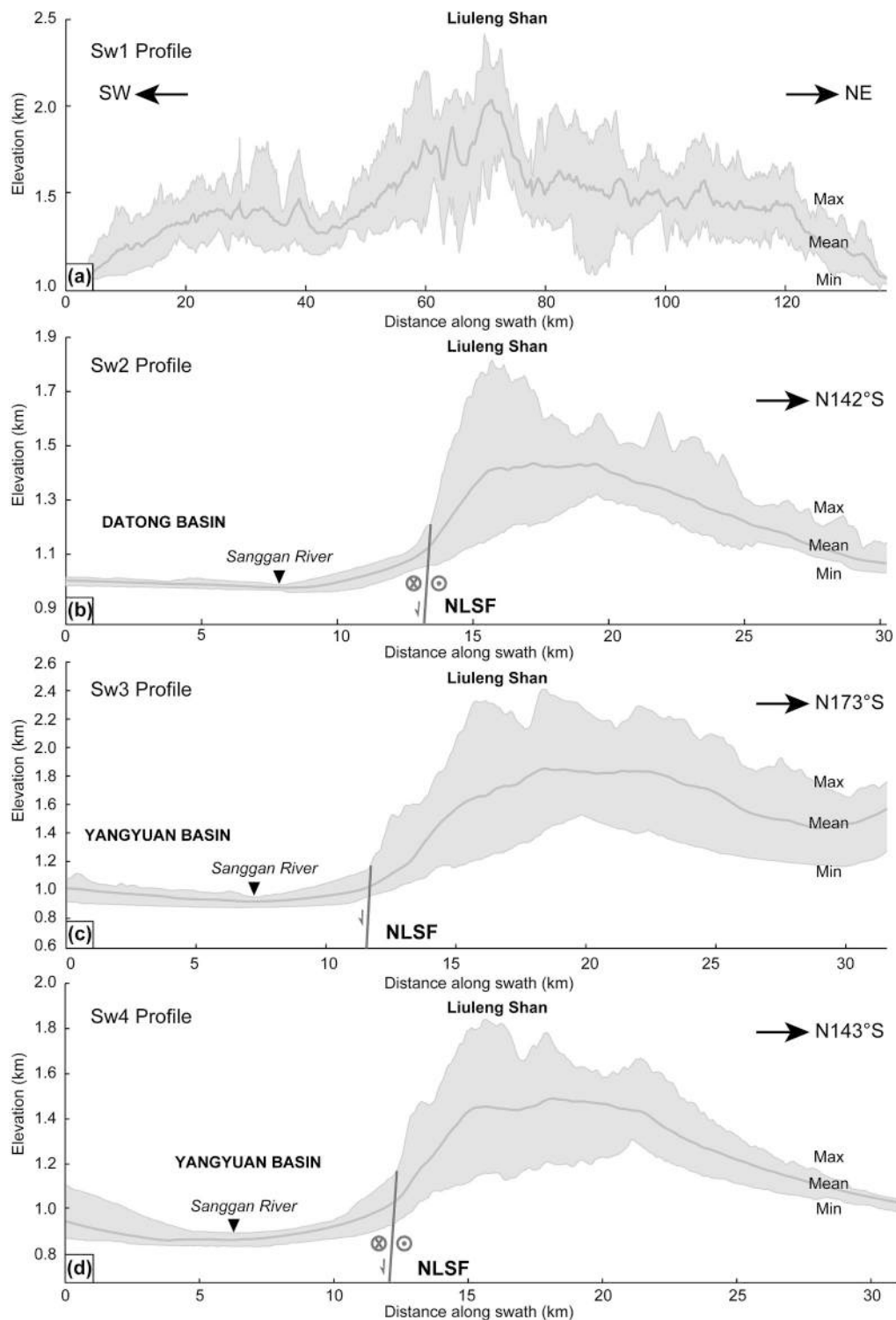


Fig. 3. Topographic swath profiles along and across the North Liuleng Shan Fault. Longitudinal Sw1 swath profile is 10 km wide and transverse Sw2-Sw4 swath profiles are 20 km wide. The location of each profile is shown in Fig. 1b.

3.1.1. Topographic swath profiles

Topographic swath profile analysis takes into account all the elevation values within a given width rather than simply measuring elevation values along an arbitrary line (Telbisz et al., 2013; Pérez-Peña et al., 2017). For each swath transect, maximum, minimum, and mean topographic elevation values within a certain width from the profile line are extracted and plotted against the distance along the swath. Mean elevation approximates the general trend of the landscape within the swath profile, while the maximum and minimum elevations can indicate the landscape variations in the direction perpendicular to the swath profile. Accordingly, topographic swath profiles have been used widely

to characterize regional-scale topography (e.g., Zhang et al., 2011). In this study, a total of four topographic swath profiles (Sw1 to Sw4) were constructed to characterize the topographic features along the Liuleng Shan (Figs. 1b and 3), using the MakeTopoSwath function in the Matlab-based Topographic Analysis Kit (TAK) software (Forte and Whipple, 2019; Schwanghart and Nikolaus, 2010; Schwanghart and Scherler, 2014). The 10 km-wide longitudinal Sw1 profile runs parallel to the mountain front and covers the Liuleng Shan bedrock mountain almost entirely. The three transverse profiles Sw2–Sw4, each 20 km wide and spanning the mountain ranges and the Datong–Yangyuan Basin, are situated in the southwest, central, and northeast portions of the Liuleng

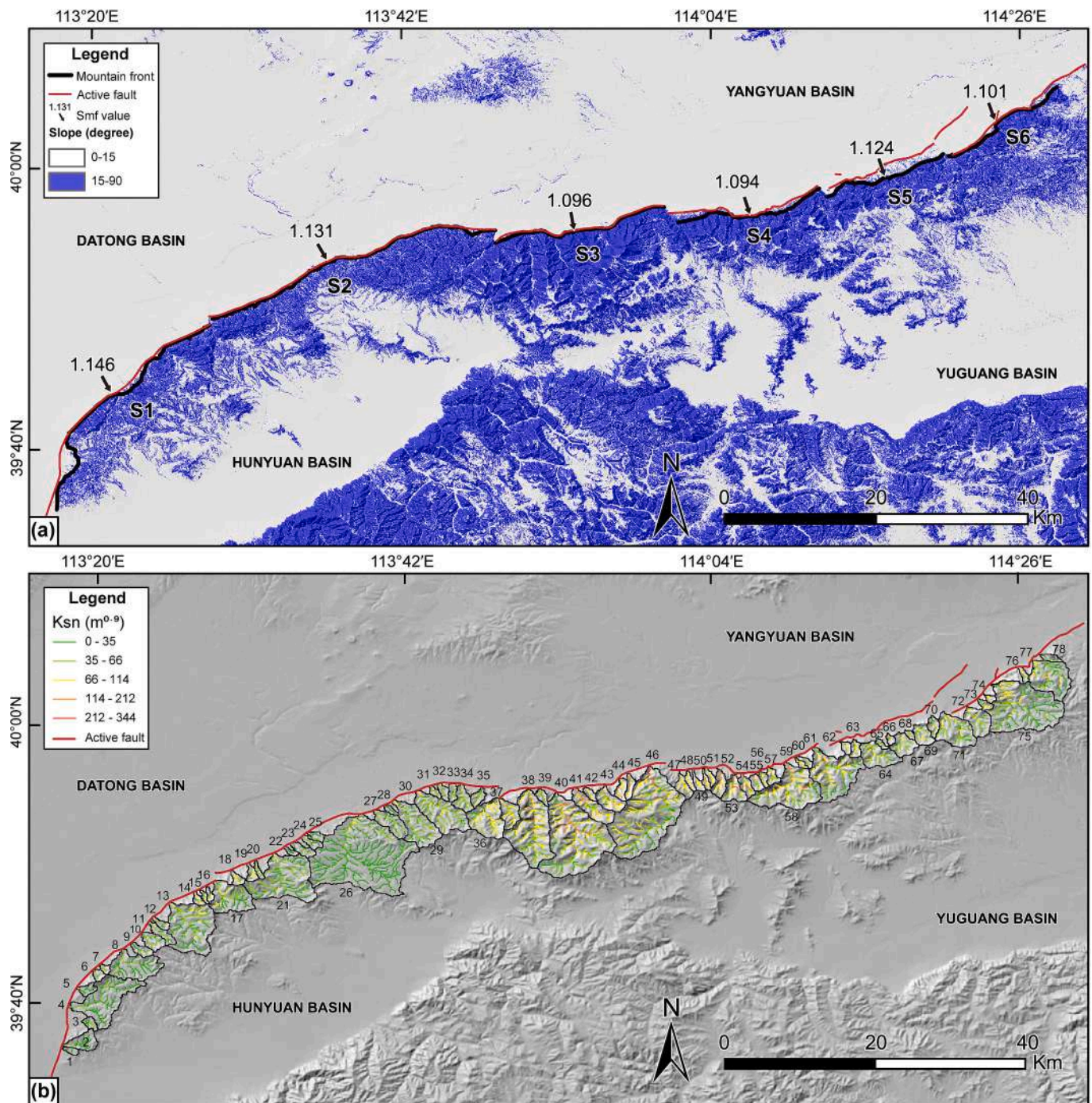


Fig. 4. Mountain front sinuosity and normalized channel steepness. (a) Hillshade map overlain by slope showing mountain-front sinuosity of the fault-bounded escarpments of the North Liuleng Shan Fault. (b) Hillshade map overlain with normalized channel steepness data. Note that the k_{sn} values of basins on the western portion (basins No.1 to No.35) are significantly smaller than those of on the central and eastern portions (basins No.36 to No.78).

Shan, respectively.

3.1.2. Mountain front sinuosity index (S_{mf})

The S_{mf} is the ratio of the length of the mountain front L_{mf} , as measured along the foot of a mountain, to the straight-line length of the mountain L_s , expressed by the equation: $s_{mf} = L_{mf}/L_s$ (Bull and McFadden, 1977). The morphology of a mountain front changes as a result of a competition between active tectonic uplift, which tends to generate and maintain a straight mountain front, and stream erosion processes, which tend to make it more irregular. Mountain fronts associated with active uplift are often straight and have low S_{mf} values (<1.4), whereas fronts tied to less active or inactive uplift will have high S_{mf} values (>1.4) (Bull and McFadden, 1977; Rockwell et al., 1985; El Hamdouni et al., 2008; Ntokos et al., 2016; Rimando and Schoenbohm, 2020).

In this work, the mountain front trace was determined using a MERIT DEM-derived slope map classified as $<15^\circ$ and $>15^\circ$ (Fig. 4a). The mountain front coincides spatially with the boundary between $<15^\circ$ and $>15^\circ$ slope values. On this basis, we manually traced the location of the mountain front in ArcGIS. We further divided the corresponding mountain front into six segments, labelled as S1 to S6, according to the segmentation of the NLSF (Fig. 4a). Unlike the S1, S2, S3, and S6 segments in which the mountain front almost overlaps with the piedmont active fault, the mountain fronts in segments S4 and S5 are separated from the fault traces by uplifted pediments with widths of 0.5–2 km. Cheng and Yang (1999) proposed that these pediments are likely the result of erosion along the shoreline of the ancient Nihewan Lake.

3.1.3. Hypsometric curve and hypsometric integral (HI)

The hypsometric curve is the ratio between the area and the altitude of a drainage basin and is created by plotting the dimensionless proportion of total basin height (h/H) against the dimensionless proportion of the total basin area (a/A). The total basin height, also known as basin relief, is defined as the maximum elevation (h_{max}) minus the minimum elevation (h_{min}). The hypsometric integral (HI) is defined as the area below the hypsometric curve (Strahler, 1952) and is expressed by the equation:

$$HI = \frac{(h_{mean} - h_{min})}{(h_{max} - h_{min})},$$

where h_{mean} is the mean elevation of a drainage basin. The shape of the hypsometric curve as well as the hypsometric value have been used to infer the stage of geomorphic development of the drainage basin. Convex hypsometric curves and high HI (>0.6) indicate a youthful stage that may be associated with active tectonic uplift; S-shaped or straight curves and intermediate values of HI ($0.3 < HI < 0.6$) indicate a mature stage, and concave curves and low values of HI (<0.3) indicate a relatively old landscape (Strahler, 1952). In this study, we plotted the hypsometric curves using the ArcGIS add-in tool, Hypsometric Integral Toolbox (available at: <https://www.arcgis.com/home/item.html?id=23a2dd9d127f41c195628457187d4a54>).

3.1.4. Valley-floor-width-to-height ratio (V_f)

V_f is used to describe the shape of the valley and is defined as the ratio of the width of the valley floor to the average height of the valley (Bull and McFadden, 1977), given by the equation:

$$V_f = 2V_{fw}/[(E_{ld}-E_{sc}) + (E_{rd}-E_{sc})],$$

where V_{fw} is the width of the valley floor; E_{ld} and E_{rd} are the elevations of the left and right valley divides, respectively; and E_{sc} is the elevation of the valley floor. Valleys with higher V_f values are often U-shaped, whereas valleys with lower V_f values are often V-shaped. V_f is a measure of the incision of a stream, however, it can also be used as a surrogate for uplift because the rate of uplift and incision is approximately equal in an equilibrium state. Therefore, low values of V_f are usually associated with higher rates of uplift and incision. In this study, the valley cross-sections used to calculate the V_f values were measured at

a distance of ~ 0.5 – 1.0 km from each basin's outlet in GlobalMapper software.

3.1.5. Asymmetry factor (A_f)

The asymmetry factor (A_f) is often used to evaluate whether or not a drainage basin is undergoing tectonic tilting (Hare and Gardner, 1985). A_f is defined by the following equation:

$$A_f = (A_r/A) * 100.$$

where A_r is the area of the basin to the right of the trunk stream (facing downstream), and A is the total area of the drainage basin. Both A_r and A values were determined directly in ArcGIS. Under the assumption of lithological uniformity, if there is little to no tilting in a drainage basin, the A_f will be close to 50. Otherwise, as the effect of tectonic tilting increases, the A_f value will deviate from 50. Therefore, the absolute values of A_f-50 (i.e., $|A_f-50|$) are more often used to evaluate relative tectonic activity (Hamdouni et al., 2008; Cheng et al., 2018). For strongly tilted basins, they will have $|A_f-50|$ values ≥ 15 , probably indicating the effects of active tectonics or strong lithological control (Hamdouni et al., 2008; Ntokos et al., 2016). Since the trunk streams of basins 10, 21, and 53 bifurcate into two channels of similar length upstream (Fig. 2a), we exclude them from our calculation of the A_f parameters.

3.1.6. Basin elongation ratio (R_e)

The Basin elongation ratio is an index used to describe the planform shape in the outline of a drainage basin (Schumm, 1956). It is a ratio of the diameter (D_c) of a circle that has the same area (A) as the basin to the drainage basin's length (L_b), given by the following equation:

$$R_e = D_c/L_b = 2(A/\pi)^{1/2}/L_b.$$

Typically, drainage basins of tectonically active mountain ranges are elongated while drainage basins of less active and inactive mountain ranges tend to be more equant (Bull and McFadden, 1977). R_e values can be influenced by climate and lithology but usually range from 0.6 to 1 (Strahler, 1964). $R_e < 0.50$ is characteristic of tectonically active basins; values ranging from 0.50 to 0.75 are slightly active basins, and $R_e > 0.75$ is inactive.

3.1.7. Normalized channel steepness index (k_{sn})

The normalized channel steepness index has been proven to be an important topographic metric for studying the relationship between topography and rock uplift in actively uplifting mountain ranges (e.g., Kirby and Whipple, 2001; Harkins et al., 2007). The fluvial reach of most graded river profiles follows an empirical power-law relationship between the local channel slope (S) and the contributing drainage area upstream (A),

$$S = k_s A^{-\theta}$$

where k_s is the channel steepness index and θ is referred to as the concavity index (mostly ranging from 0.4 to 0.6) (Hack, 1957; Flint, 1974; Kirby and Whipple, 2012). Using a reference concavity index (θ_{ref}), one can determine a normalized steepness index (k_{sn}) that allows effective comparison of profiles of streams with varying drainage areas (Wobus et al., 2006):

$$S = k_{sn} A^{-\theta_{ref}}$$

On a theoretical basis, the elevation (Z) at a point in a channel evolves with time following the stream power incision model (Whipple and Tucker, 2002; Wobus et al., 2006):

$$\frac{\partial Z}{\partial t} = U - E = U - K A^m S^n$$

where U is the rate of rock uplift, E is the erosion rate, K is the erosional coefficient set by climate, rock erodibility, and channel geometry, and m and n are empirical constants. At steady state ($\frac{\partial Z}{\partial t} = 0$ or $U = E$) and

assuming uniform U and K , the following relationship can be derived:

$$S = \left(\frac{U}{K}\right)^{\frac{1}{n}} A^{-\frac{m}{n}}$$

Therefore,

$$\theta = \frac{m}{n}$$

and

$$k_s = \left(\frac{U}{K}\right)^{\frac{1}{n}}$$

This formula indicates a positive relationship between k_{sn} and rock uplift rate U under the assumption that K and n do not vary in time and space.

In our study, we follow many other studies in setting $\theta = \theta_{ref} = 0.45$ (e.g., Kirby et al., 2003; DiBiase et al., 2010; Rimando and Schoenbohm, 2020) and adopt a smoothing window of 500 m to acquire a k_{sn} -map (Fig. 4b) through regressions of channel gradient and drainage area using the KsnChiBatch function in the TAK software (Forte and Whipple, 2019; Schwanghart and Nikolaus, 2010; Schwanghart and Scherler, 2014). We calculate and plot basin-averaged k_{sn} values versus the distance along the fault to interpret the spatial distribution patterns of relative uplift rates.

3.2. Fault characterization

Active faulting along the NLSF is well expressed at the surface by its geomorphology. In this study, we used a combination of field geological surveys and interpretation of UAV-based photogrammetry data to better characterize the geomorphic features associated with the NLSF. The field sites were chosen mainly based on the interpretation of Google Earth satellite images, but we also revisited some sites that were described in previous studies. We selected sites with well-preserved displaced geomorphic features to conduct a detailed study. We used SfM-based UAV photogrammetry (e.g., Johnson et al., 2014) to produce high-resolution DEMs (~ 0.2 m/pixel) that were then used to map and measure the magnitude of offset on displaced geomorphic surfaces. The mapping and determination of the relative ages of different levels of geomorphic surfaces (i.e., alluvial fans and fluvial terraces) were mainly based on field observations of depositional characteristics and the measurement of heights above modern streams. We used the Matlab-based software, PointFit v14 (Li et al., 2022; available at <https://github.com/AMSunip/PointFit>), to quantify the heights of scarps by extracting topographic profiles perpendicular to the fault scarps. Fault lateral offset was measured on the DEM data by using piercing points associated with offset geomorphic markers (e.g., terrace risers).

4. Results

4.1. Geomorphic analysis

Our geomorphic analysis reveals significant along-strike changes in the topography of the footwall block of the NLSF. The along-strike swath profile (Sw1) shows that the Liuleng Shan reaches higher elevations in the central portion and decreases in elevation to the southwest and northeast (Fig. 3a). The three transverse swath profiles (Sw2-Sw4) mainly reflect the relief between the mountain and the basin (Figs. 3b-3d). This relief is greater in the central part of the NLSF, reaching about 1400 m in difference in maximum topography between the basin and peak of the range, and tapers to 800 m to the southwest and 900 m to the northeast.

S_{mf} values for all six of the mountain front segments are between 1.094 and 1.146 (Fig. 4a) and are smaller than 1.4, which fall within the range of values reflecting active faulting (Bull and McFadden, 1977;

Small and Anderson, 1998). Values in the S3 and S4 segments in the central portion of the NLSF are lower than those in the western (S1 and S2 segments) and eastern portions (S5 and S6 segments) of the fault zone.

We plotted drainage basin-based geomorphic indices against distance from the southwestern fault tip to reveal potential along-strike variations (Fig. 5). Basin relief is a maximum in the S3 segment (~ 1400 m) in the central portion of the NLSF and decreases toward the two ends of the range (Fig. 5a), which is similar to the trend exhibited by the maximum elevation documented in the transverse swath profiles. Basin-averaged slopes also show a consistent along-strike trend with higher values in the central portion of the range and lower values to the northeast and southwest (Fig. 5b). The basin-averaged slope of the S3 and S4 segments is $22.86 \pm 3.21^\circ$, while those of the S1 and S2 segments in the southwest and the S5 and S6 segments in the northeast are $14.90 \pm 3.56^\circ$ and $18.58 \pm 3.12^\circ$, respectively.

Hypsometric Integral (HI) values vary between 0.37 and 0.65 and do not show any obvious dependence on catchment area or shape (Figs. S1 and S2). A comparison of the HI values of drainage basins in Yan et al. (2011) with those determined in this study shows that they are in good agreement (Fig. S3). Additionally, HI shows an increase in values from southwest to northeast along the mountain range (Fig. 5c). The hypsometric curves exhibit a similar trend (Fig. 6): drainage basins in the S1 segment have S-shaped hypsometric curves; the curves of drainage basins on the S2 segment are mainly S- and concave-shaped, except for basin No.18 which has a convex-shaped curve; for drainage basin in the S3 and S4 segments, the hypsometric curves are mostly straight lines or convex-shaped; while for the S5 and S6 segments, S-shaped and convex hypsometric curves are observed.

Valley floor width-to-height ratio (V_f) values range from 0.25 to 3.03. Drainage basins with low V_f values are mostly located in the S3 and S4 segments in the central portion of the fault (Fig. 5d). We calculated mean V_f values of 1.20 ± 0.67 , 0.61 ± 0.29 , and 1.14 ± 0.52 for the S1-S2, S3-S4, and S5-S6 segments, respectively. Asymmetry factor $|A_f - 50|$ values range from 1 to 31, however, there is no noticeable spatial trend (Fig. 5e). Elongation ratio (R_e) values range from 0.4 to 0.9, with the elongated drainage basins being more abundant along the S3 and S4 segments at the center of the fault, especially within the S4 segment (Fig. 5f). In contrast, we document drainage basins with increasingly equant morphologies more abundant along the southwestern and northeastern portions of the fault, especially in the S1 and S2 segments. We calculated mean R_e values of 0.65 ± 0.10 , 0.59 ± 0.11 , and 0.68 ± 0.10 for the S1-S2, S3-S4, and S5-S6 segments, respectively. Basin-averaged k_{sn} is higher in the center of Liuleng Shan (77.22 ± 13.28 m^{0.9}) than in the southwestern and northeastern portions of the range (39.51 ± 12.92 , and 52.45 ± 10.82 m^{0.9}, respectively) (Fig. 5g).

4.2. Fault observations

Previous studies documented dextral strike-slip along the NE-striking S1 and S6 segments of the NLFZ (Luo et al., 2022a, 2022b). In this work, we report new geomorphic data for the other fault segments, finding evidence for strike-slip motion on the NE-striking S2 segment, and dip-slip, normal displacement on the E-W striking segments S3, S4, and S5 (Fig. 1b).

The S2 fault segment in the vicinity of Nanmiyao village consists of two fault strands (Fig. 7a). The southern strand, evidenced by a series of northwest-facing triangular facets, forms the boundary between the uplifted bedrock mountain and the downthrown basin. The northern strand, on the other hand, is located ~ 200 m north of the southern strand in the basin and exhibits linear fault scarps with a maximum height of ~ 6 m. Mapping of displaced geomorphic features reveals that the fault also shows right-lateral strike-slip displacement (Fig. 7b). Two northwestward flowing stream channels, R1 and R2, are deflected right-laterally at the location of the fault. Fluvial terraces flanking these two channels have also been displaced right-laterally by the fault. Offset

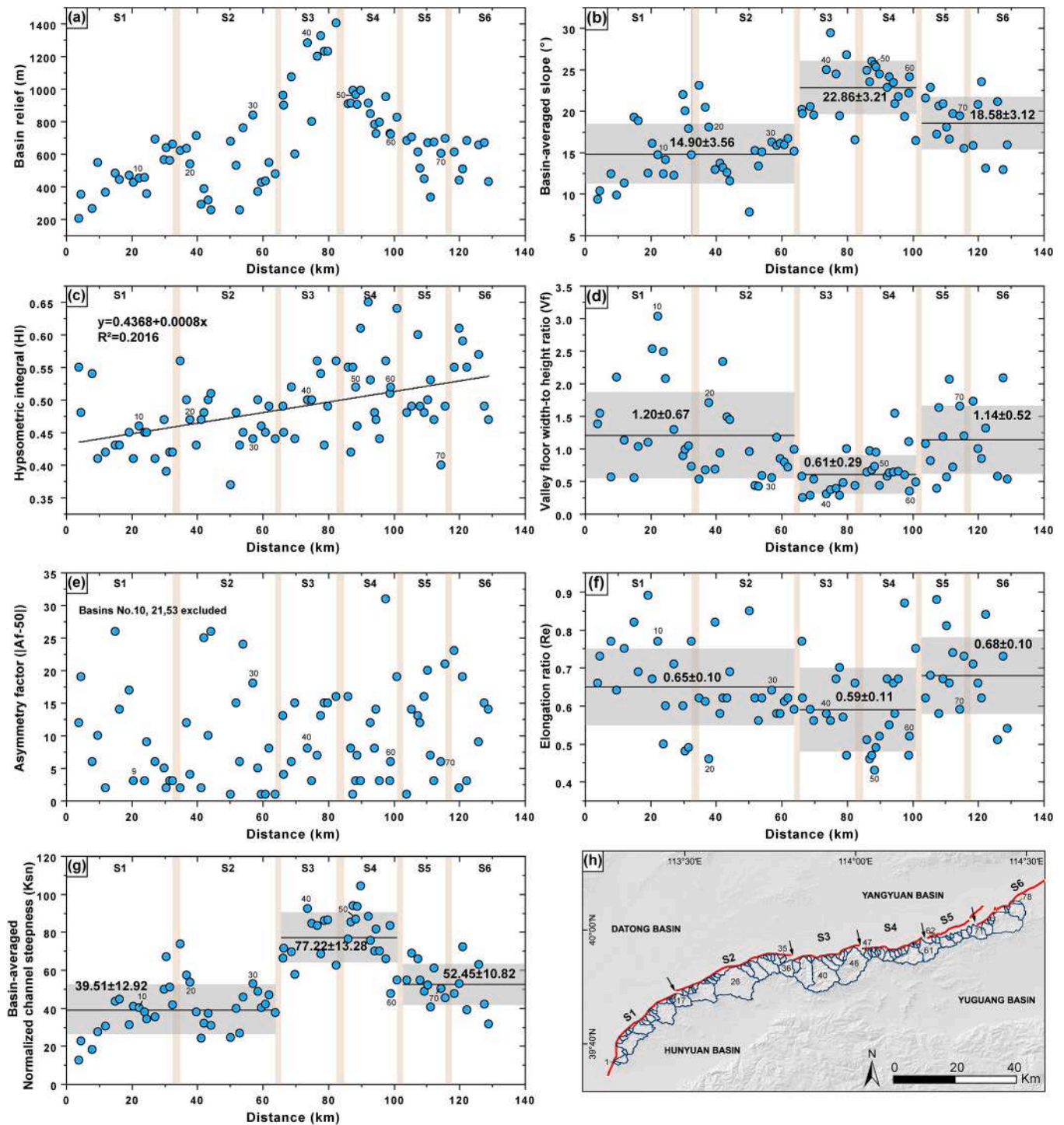


Fig. 5. Determined drainage basin-based geomorphic indices. Data is referenced in Table S1. (a-g) Distributions of the basin relief, basin-averaged slope, hypsometric integral, valley floor width-to-height ratio, asymmetry factor, elongation ratio, and basin-averaged normalized channel steepness, respectively. Light brown shaded rectangular areas indicate fault segment boundaries. (h) Hillshade map showing fault trace (red line), drainage basin (polygons), and fault segmentation (black arrows). (For interpretation of the references to colour in this figure legend, the reader is referred to the web version of this article.)

magnitudes of ~ 10 m were measured for the T_2 and T_2' terraces. In the vicinity of Mijiayao village, also along the S2 fault segment, five levels of fluvial terraces (T_4 , T_3 , T_2' , T_2 , and T_1 from old to young) are developed along the flanks of the northward flowing R_3 stream channel (Fig. 8a and b). The T_3/T_2 terrace riser is displaced right-laterally by about 13.2 m (Fig. 8b and c). In addition to the lateral offset, the T_3 terrace also shows vertical displacement, but the amount cannot be determined because of human modification (Fig. 8a and b). The T_2 terrace is not significantly

displaced horizontally or vertically. The fault crops out in the west wall of the stream channel, marked by vertical displacement of the loess-gravel contact along with oriented gravels indicative of fault displacement (Fig. 8d). This provides convincing evidence that the offset of the T_3/T_2 terrace riser is related to faulting. Based on the observations, the S2 fault segment exhibits dextral transensional faulting.

Our data support earlier interpretations that the S3, S4, and S5 segments of the NLSF are characterized by normal faulting (Deng et al.,

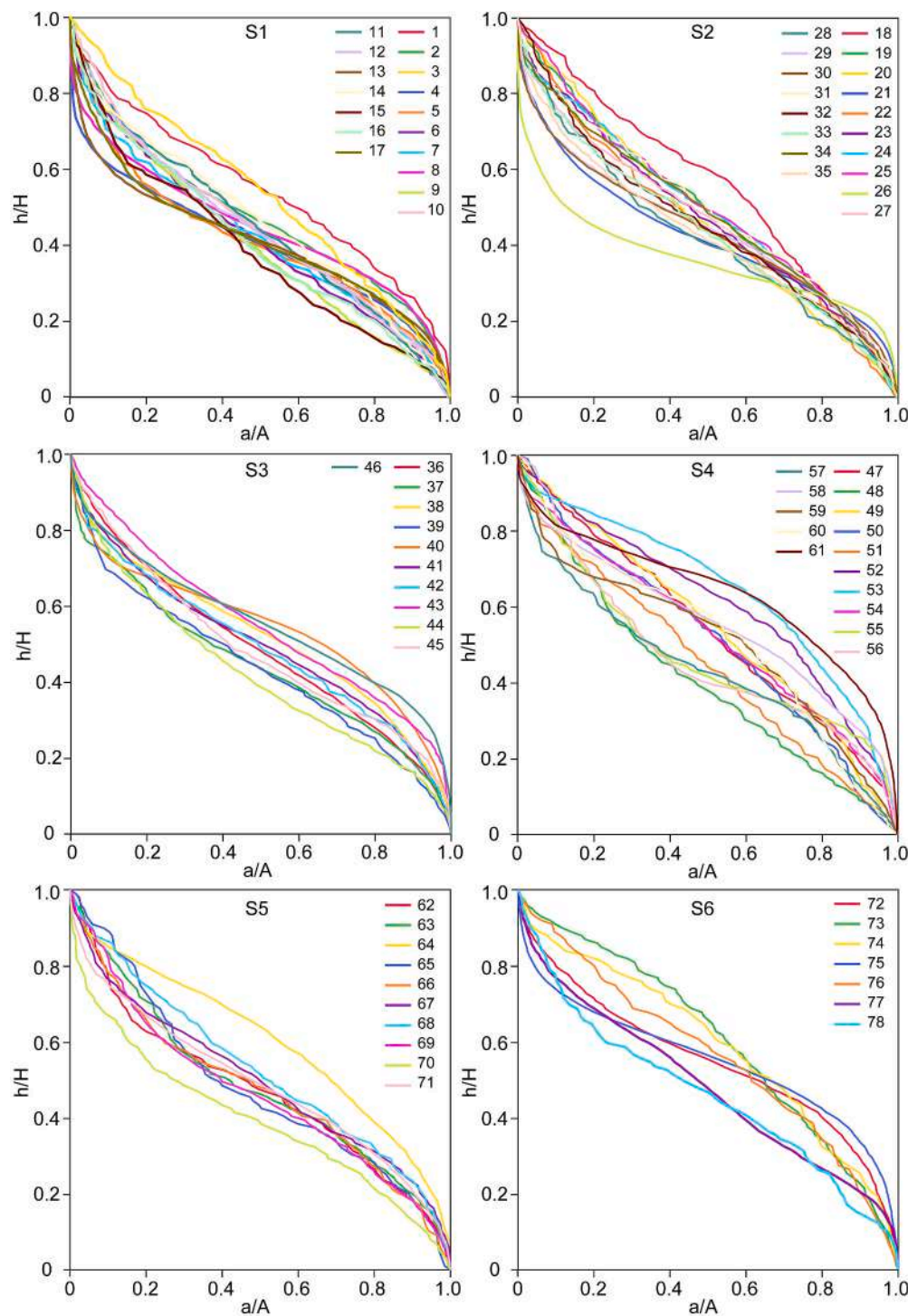


Fig. 6. Hypsometric curves for all segments of the Liuleng Shan mountain fronts. Segment boundaries are indicated in Fig. 5h.

1994; Duan and Fang, 1995; Xu et al., 1996b; Sun, 2018). Along the fault trace of the S3 segment in the vicinity of Xituanbu village, we observe magnificent triangular facets (Fig. 9a). We also document the offset of a Quaternary basalt with a K—Ar age of 0.68 ± 0.13 ka and 30–50 m-high fault scarps along this fault segment (Fig. 9b; Deng et al., 1994; Xu et al., 1996a; Shi et al., 2020a). Fault segments S4 and S5 are mainly located in front of uplifted pediments, forming impressive linear fault scarps (Fig. 9c and d). For example, in the vicinity of Shangzhuang village on the S4 segment, the fault mainly manifests as continuous near-east-west striking fault scarps with heights that range from 13 to 32 m (Fig. 10). Stream channels do not exhibit any strike-slip displacement. In the

vicinity of Gaojiayao village along the S5 segment, four levels of fluvial terraces (T_4 to T_1 from old to young) are developed at the outlet of drainage basin No.68. The T_3 and T_4 terraces display obvious vertical offset, forming ~6 m and ~16–23 m high fault scarps, respectively (Fig. 11). Xu et al. (2002) reported that the T_2 terrace was also faulted, however, the fault scarps are already hard to distinguish due to human agricultural activity. A trench across fault scarps on the T_3 terrace indicates at least two seismic events during the Holocene (Xu et al., 2002). Neither the terrace riser nor the stream channels show signs of lateral displacement at this locality.

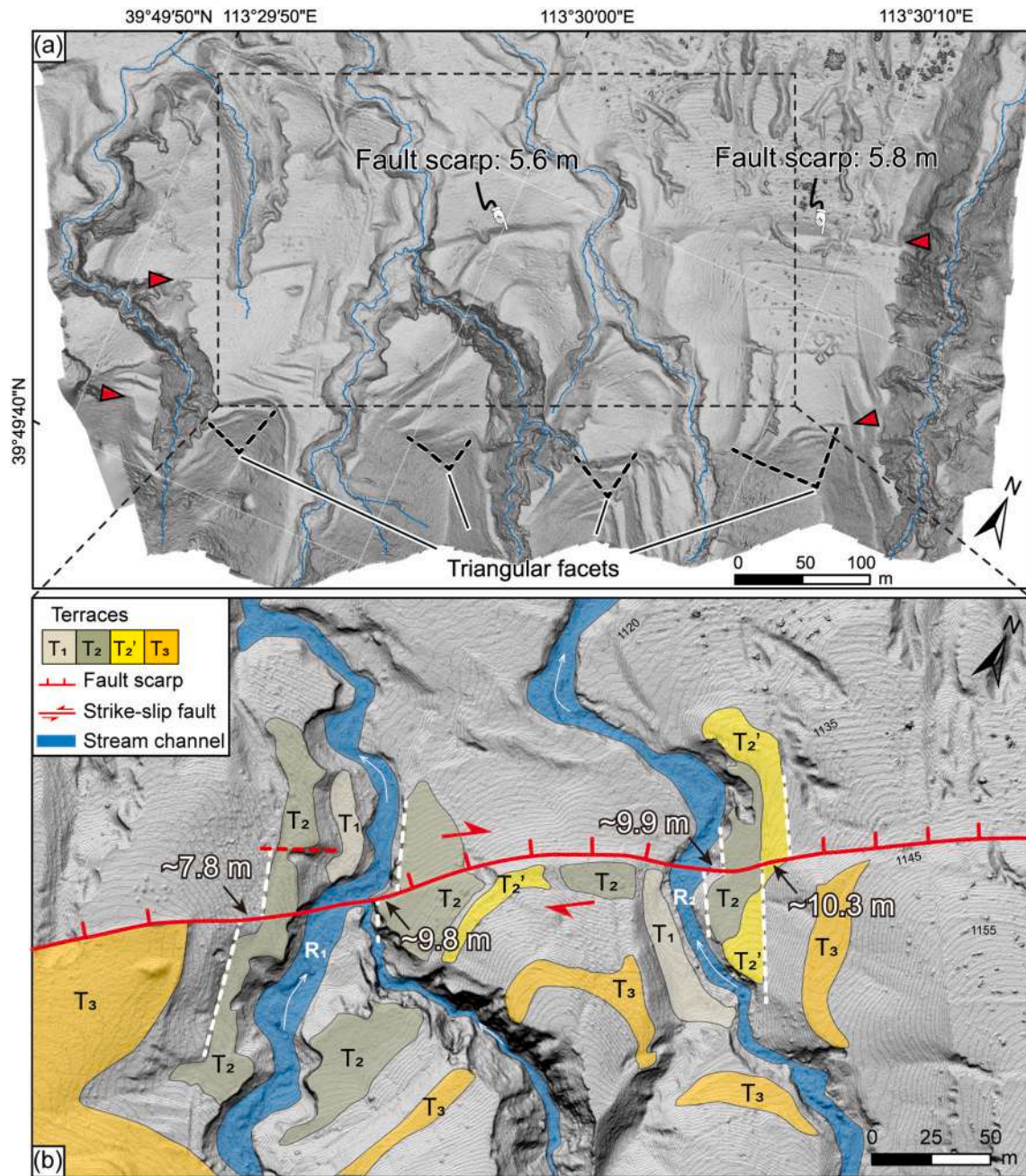


Fig. 7. Displaced geomorphic features along the S2 fault segment in the vicinity of Nanmiyao village, with the location shown in Fig. 1b. (a) Hillshade map showing fault traces (red triangles). (b) Hillshade map overlain by 0.5 m-interval topographic contours showing fluvial terrace staircases, fault trace (red line), fault scarps (red teeth), and right-laterally displaced channels and terrace risers. The dashed red line indicates a fault trace with uncertainties. (For interpretation of the references to colour in this figure legend, the reader is referred to the web version of this article.)

5. Discussion

5.1. Synthesis of kinematic and geomorphic data along the NLSF

5.1.1. Geomorphic data

Our analysis of geomorphic indices reveals that the relative uplift rate is non-uniform along the NLSF. Higher basin-averaged slopes and k_{sn} , coupled with lower V_f , R_e , and S_{mf} values (Figs. 4 and 5), support an interpretation that the S3 and S4 segments in the central portion of the fault system are experiencing higher uplift rates than the southwestern and northeastern fault segments. The combination of geomorphic indices such as S_{mf} and V_f values can also be used to indicate relative tectonic activity levels of the related mountain fronts (Silva et al., 2003;

Yıldırım, 2014; Yazıcı et al., 2018; Saber et al., 2018). Following Silva et al. (2003), we calculated the average V_f and standard deviation for each mountain front (Table S2) and plotted them against S_{mf} values (Fig. 12). Our data conform to a logarithmic regression line: $V_f = 14.603 \cdot \ln(S_{mf}) - 0.6069$, with a coefficient of determination (R^2) of ~ 0.6 , consistent with the relationship of $V_f = A \cdot \ln(S_{mf}) - B$ for normal-faulted mountain fronts (Silva et al., 2003). According to Rockwell et al. (1985), highly active fronts consistently produce lower values of S_{mf} and V_f . Our data thus indicate that segments S4 and S3 in the central portion of the fault system experience higher uplift rates than segments S6 and S5 in the northeast, followed by segments S2 and S1 in the southwest. This order is also consistent with the trends reflected by the single geomorphic parameter such as slope, V_f , R_e , and k_{sn} (Fig. 5).

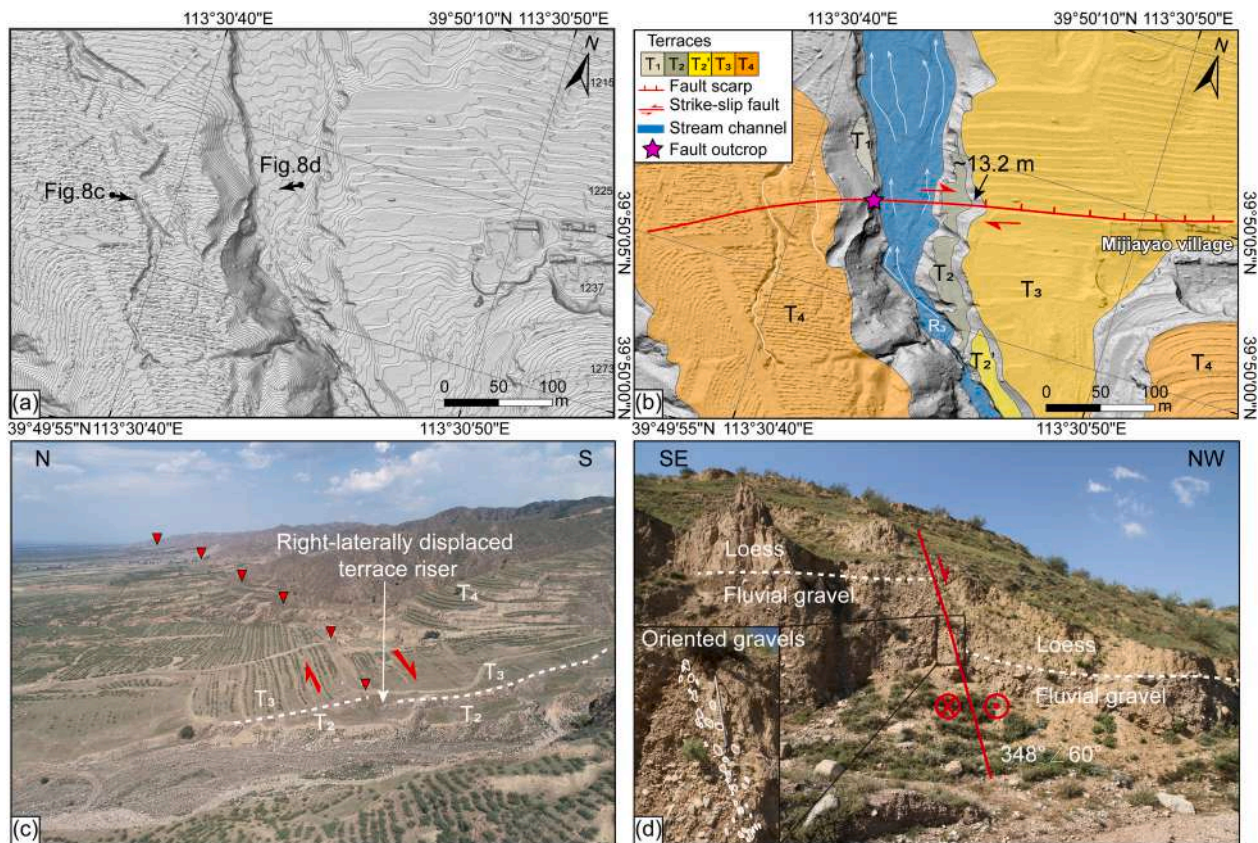


Fig. 8. Displaced geomorphic features along the S2 fault segment in the vicinity of Mijiayao village, with the location shown in Fig. 1b. (a) Hillshade map overlain by 1.0 m-interval topographic contours and (b) interpreted map showing fluvial terrace staircases, fault trace (red line), fault scarps (red teeth), and right-laterally displaced terrace riser. (c) Field photo showing the overall topography and the right-laterally displaced T_3/T_2 terrace riser. (d) Field photo showing a fault outcrop in which fluvial gravels were dragged parallel with the fault plane. (For interpretation of the references to colour in this figure legend, the reader is referred to the web version of this article.)

Furthermore, according to the classification of Rockwell et al. (1985), segments S3 and S4 are within tectonic activity Class 1 ($S_{mf} < 1.4$ and $V_f < 1$), which corresponds to inferred uplift rates of at least 0.4–0.5 mm/yr. Contrary to the view of Cheng and Yang (1999) that the NLSF as a whole consists of two segments with different levels of tectonic activity, we suggest that the NLSF can be divided into three segments based on the level of activity: a faster uplifting central segment and two slower uplifting southwestern and northeastern segments, in terms of vertical motion alone.

We also note that our HI and $|A_f-50|$ values do not exhibit characteristics similar to the other geomorphic indices (Fig. 5). From southwest to northeast, HI values increase (Fig. 5c), and the hypsometric curves also change from S-shaped and concave-shaped to straight line and convex-shaped (Fig. 6). These observations suggest that the maturity of the landscape decreases from southwest to northeast. There is no spatial trend in the asymmetry factor data. As mentioned earlier, hypsometric integral and asymmetry factors do not directly indicate relative uplift rates. They are not like geomorphic indices such as S_{mf} and V_f , measured at or near the interface of the mountain range and the piedmont where tectonic perturbations originate (Rimando and Schoenbohm, 2020).

Differences in lithology may also cause spatial variations in geomorphic parameters, so they need to be taken into account. We examined the publicly available 1:200,000 digital geological maps (Li et al., 2017; <http://dgc.cgs.gov.cn/cn/geologicalData/details/doi/10.23650/data.A.2019.NGA120157.K1.1.1.V1>) of the study area to assess the potential role of lithologic resistance in influencing the measurement of geomorphic indices. The different rock types presented along the drainage basin in the Liuleng Shan include Archean metamorphic rocks, Proterozoic and Early Paleozoic carbonate rocks, Mesozoic granitic

intrusions, and also Jurassic and Cenozoic sedimentary rocks (Fig. 2a). However, lithology does not appear to exert significant control over geomorphic indices. For example, the basal lithology of the drainage basins in the southwestern section is mainly Archean metamorphic rocks, but the geomorphic indices (e.g., the basin-averaged slope, k_{sb} , V_f) of this section show considerable variability. Similarly, although drainage basins in the northeastern section of the range uniformly consist of Sinian and Carboniferous limestone and dolomite, the determined geomorphic indices vary from basin to basin in the northeastern section. In contrast, despite varying lithology in the S3 and S4 segments on the central portion, geomorphic indices return relatively consistent values. Lithology is also unlikely to be responsible for the trend of HI values, as the gneisses and granites in the southwestern and central portion of the Liuleng Shan have higher erosional resistance than that of the dolomite and limestone in the northeastern portion (Selby, 1980; Yildirim, 2014). If lithology affects basin hypsometry, the trend should be reversed. However, we acknowledge that lithology may have influenced the slopes of basins No.40–44, which are located in the central part of the Liuleng Shan and have the highest slopes among all basins (Fig. 5b). These basins are underlain by granite, which has a high rock erosional resistance (Fig. 2a). Furthermore, the topography of the Liuleng Shan and the relief of the basins are also at their maximum in this region (as shown in Figs. 3 and 5a). We believe that these effects are localized because overall the slope, basin relief, and topography increase from the ends to the central. More importantly, the other geomorphic parameters of basin No.40–44 do not exhibit features that clearly distinguish them from adjacent basins. Both scenarios suggest that lithology is not a dominant factor controlling the distribution of geomorphic indices.

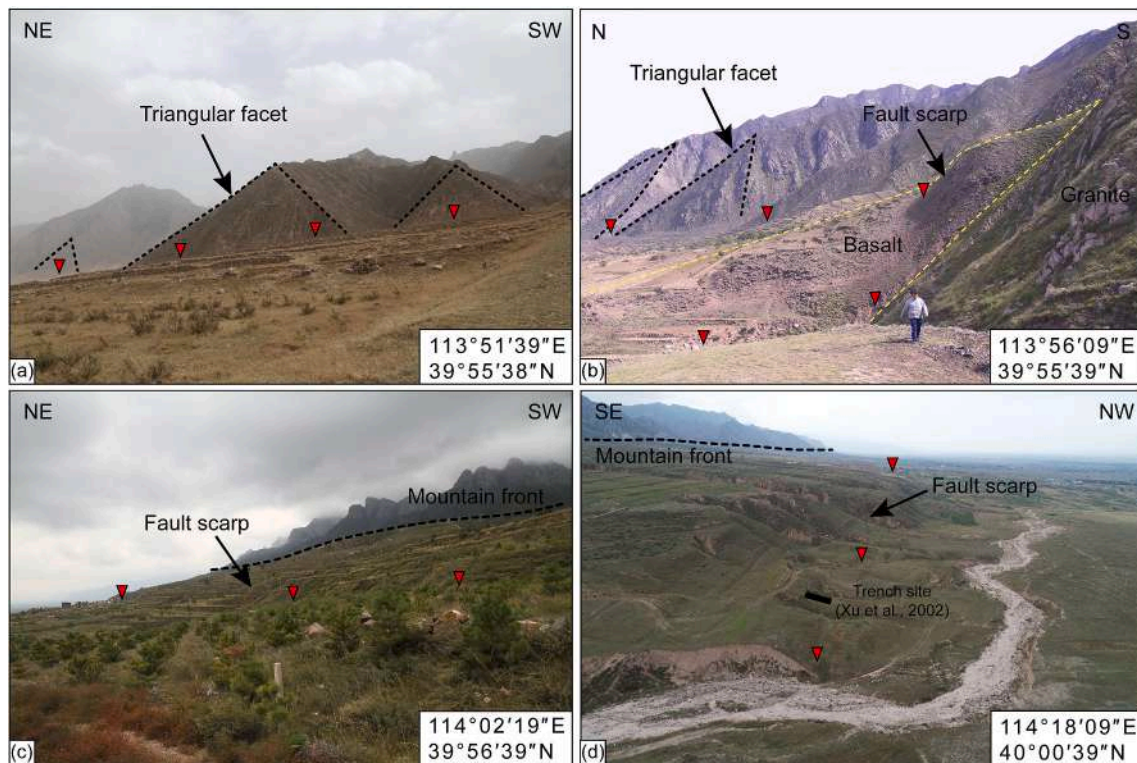


Fig. 9. Field photos showing displaced geomorphic features along the S3, S4, and S5 fault segments. (a) Triangular facets in the vicinity of Xitubu village. (b) Faulted basalt in the vicinity of Qiulin village. (c) Fault scarps in the vicinity of Shangzhuang village. (d) Faulted terraces in the vicinity of Gaojiayao village. Red triangles indicate the fault trace. The locations of the photos are shown in Fig. 1b, Fig. 10, and Fig. 11. (For interpretation of the references to colour in this figure legend, the reader is referred to the web version of this article.)

Climate may affect geomorphic data as well. We use present climatic data to evaluate the role of climate in geomorphic evolution because detailed long-term paleo-climatic data are not available here. Mean annual precipitation in the analyzed drainage basins ranges from 360 to 460 mm/yr, averaging 397 ± 47 mm/yr (Fig. 2b; <http://www.worldclim.org/version2>). Although a few drainage basins in the central segment of the fault system receive higher precipitation than others, the relatively small absolute difference likely has a limited impact on the significant differences in geomorphic parameters. To test this, we plotted the geomorphic indices against mean annual precipitation data, yielding a very low correlation (Fig. S4). Given the small spatial extent of the study area (spanning just over 100 km from west to east), it is reasonable to believe that the role of climatic conditions in the past is also very limited.

5.1.2. Fault geometry and kinematics

Both previously published work and fault kinematic determinations in this study reveal that the kinematic features of the NLSF are variable with fault strike. In plan view, the NLSF is composed of three sections with different strikes (Fig. 1b): the NNE and NE striking S1 and S2 segments in the southwest, the EW striking S3 and S4 segments in the center, and the NE-striking S5 and S6 segments in the northeast. The S1 segment is characterized by right-lateral oblique-slip movement, with right-lateral strike-slip rates of ~ 1.6 mm/yr (Deng and Xu, 1995; Xu et al., 1996b; Luo et al., 2022a). In this study, we report evidence of right-lateral strike-slip on the S2 segment, which includes offset stream channels and terrace risers. Combined with previous work (e.g., Deng et al., 1994), we conclude that the S2 segment is also characterized by right-lateral oblique-slip movement. In contrast, previously published work and this study find that the S3, S4, and S5 segments are normal-faulting-dominated (Deng et al., 1994; Duan and Fang, 1995; Xu et al., 1996a; Sun, 2018). Finally, Luo et al. (2022b) concluded that the S6

segment also exhibits right-lateral oblique slip with magnitudes of lateral slip rate of 0.2–0.3 mm/yr. In their work, the dextral-slip evidence involves offset stream channels and terrace risers, and fault striations that are related to slip events in the late Quaternary. Many geological constraints on vertical slip rates of the NLSF have been obtained (Deng et al., 1994; Duan and Fang, 1995; Xu et al., 1996a; Sun, 2018; Luo et al., 2022a, 2022b). We compile and plot them in Table S3 and Fig. 13 (data without age constraints have been excluded), respectively. These data are scattered and even vary at the same site, possibly due to the inconsistent timescales the different geomorphic markers represent. In addition, there is little data in the central portion of the fault system. However, there appears to be an increasing trend in vertical slip rate toward the center of the fault system, consistent with our analysis of geomorphic indices.

In summary, we find evidence for dominantly strike-slip displacement and relatively low values of vertical displacement on the northeastern and southwestern ends of the NLSF (segments S1, S2, and S6). In contrast, there is abundant geomorphic data and slip-rate measurements that indicate a greater component of vertical displacement in the central section of the fault system (S3 and S4). We would anticipate right-lateral strike-slip along the S5 segment, as the geomorphic parameters of this segment are quite similar to those of the S6 segment. However, based on the available field data, the S5 segment is dominated by normal faulting. Nevertheless, given that the S5 and S6 segments have the same fault strike, we cannot rule out the possibility of a component of right-lateral strike-slip along the S5 segment. In addition, hypsometric data suggest decreasing landscape maturity toward the northeast along the fault system, suggesting that the timing of fault initiation may be different from the current pattern of uplift.

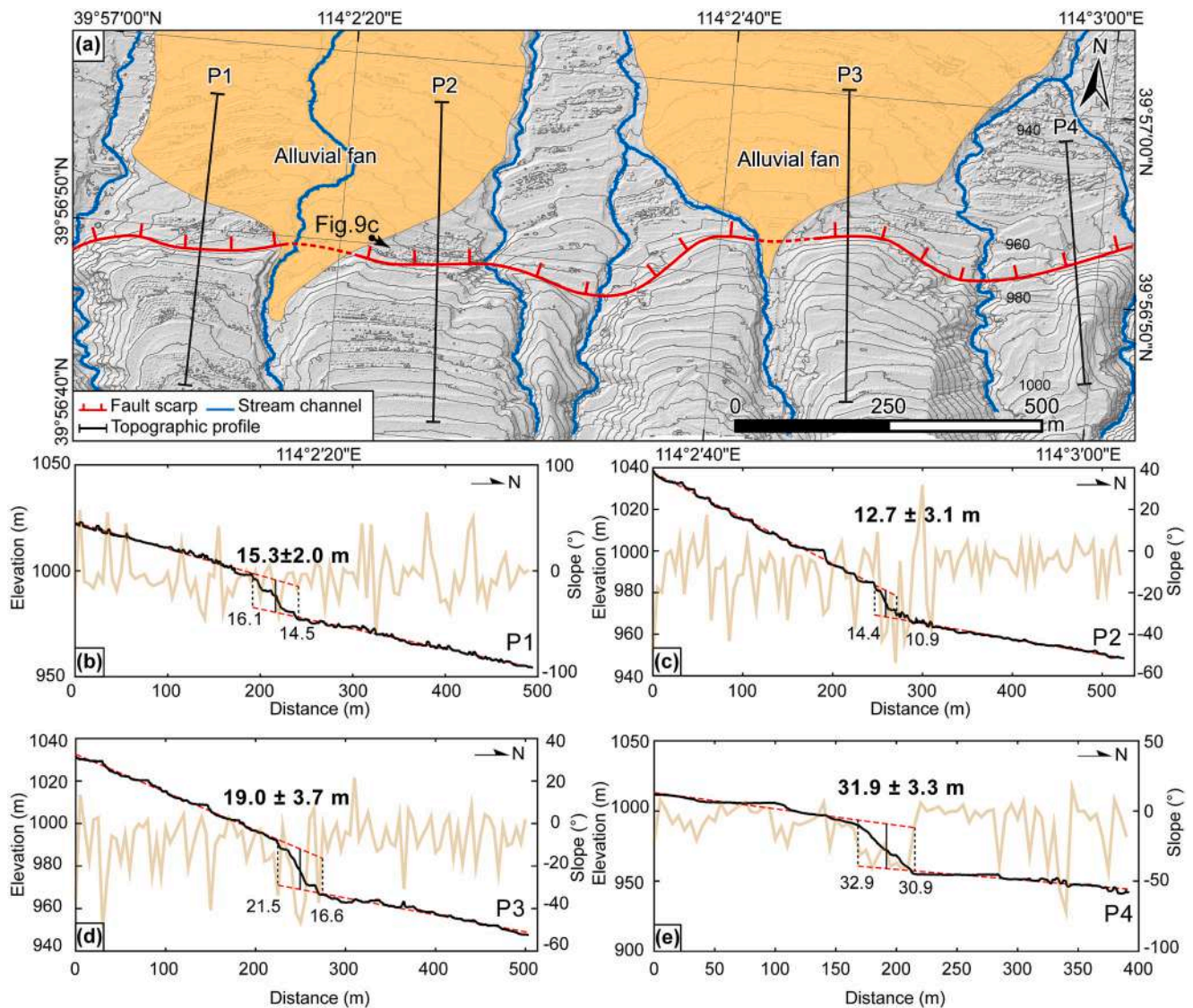


Fig. 10. Topographic map and profiles showing displaced geomorphic features in the vicinity of Shangzhuang village, with location shown in Fig. 1b. (a) Hillshade map overlain by 5 m-interval topographic contours showing fault traces (red line), fault scarps (red teeth), and locations of topographic profiles. (b–e) Topographic profiles and slope profiles with locations are indicated in Fig. 10a. (For interpretation of the references to colour in this figure legend, the reader is referred to the web version of this article.)

5.2. Active deformation pattern of the NLSF

As discussed above, neither lithology nor climate is the primary determinant of the spatial distribution of geomorphic indices along the NLSF and their pattern, therefore, most likely results from tectonic forces. Given the along-strike variations in fault geometry and kinematics, we propose here that the deformation of the NLSF conforms to a right-lateral oblique-slip releasing bend model (Fig. 14; Cunningham and Mann, 2007). Geometrically, both the southwestern and northeastern portions of the NLSF strike NE and are arranged in a right-stepping en-echelon style. Kinematically, they are both oblique right-lateral faults. Consequently, a releasing bend is found between them at the location of the E-W-striking, normal-faulting-dominated central portion of the NLSF. The southwestern portion of the NLSF, with a relatively high dextral strike-slip rate (~ 1.6 mm/yr), has long been considered as part of the dextral shear zone of the SGS (Xu and Ma, 1992; Deng and Xu, 1995; Deng et al., 1999). The dextral strike-slip rate of the northeastern portion of the NLSF, which is far from the main body of the dextral shear zone of the SGS, is significantly lower (0.2–0.3 mm/yr). We argue that this decrease in dextral slip is mainly accommodated

by extension along the central portion of the fault, a mechanism that also occurs along the Death Valley Fault Zone (DVFZ) in the Eastern California Shear Zone of the Basin and Range province, USA (Pardo et al., 2012). Our interpretation coincides with the higher relative uplift rate in the central portion of the NLSF compared to lower uplift rates in the southwestern and northeastern portions as revealed by our geomorphic data (Fig. 5) and vertical uplift rate compilation (Fig. 13). Right-lateral slip along the southwestern part of the NLSF is not completely absorbed by extension along the central NLSF and the remaining slip contributes to the right-lateral slip along the northeastern portion of the NLSF. This model explains why the northeastern NLSF has a relatively large vertical movement along with a right-lateral slip component. Future work needs to quantify the vertical slip rate of the central portion of the NLSF.

Fault bends can change the stress state and affect strain partitioning around them, and may provide nucleation sites for major earthquakes (King and Nabelek, 1985; Wang et al., 2017). The 1989 Datong-Yanggao earthquake swarm occurred within the releasing bend zone we identified (Fig. 1b), raising the question of whether the bend influenced the nucleation of the earthquake swarm. In addition, releasing bends are associated with crustal extension, thereby potentially creating

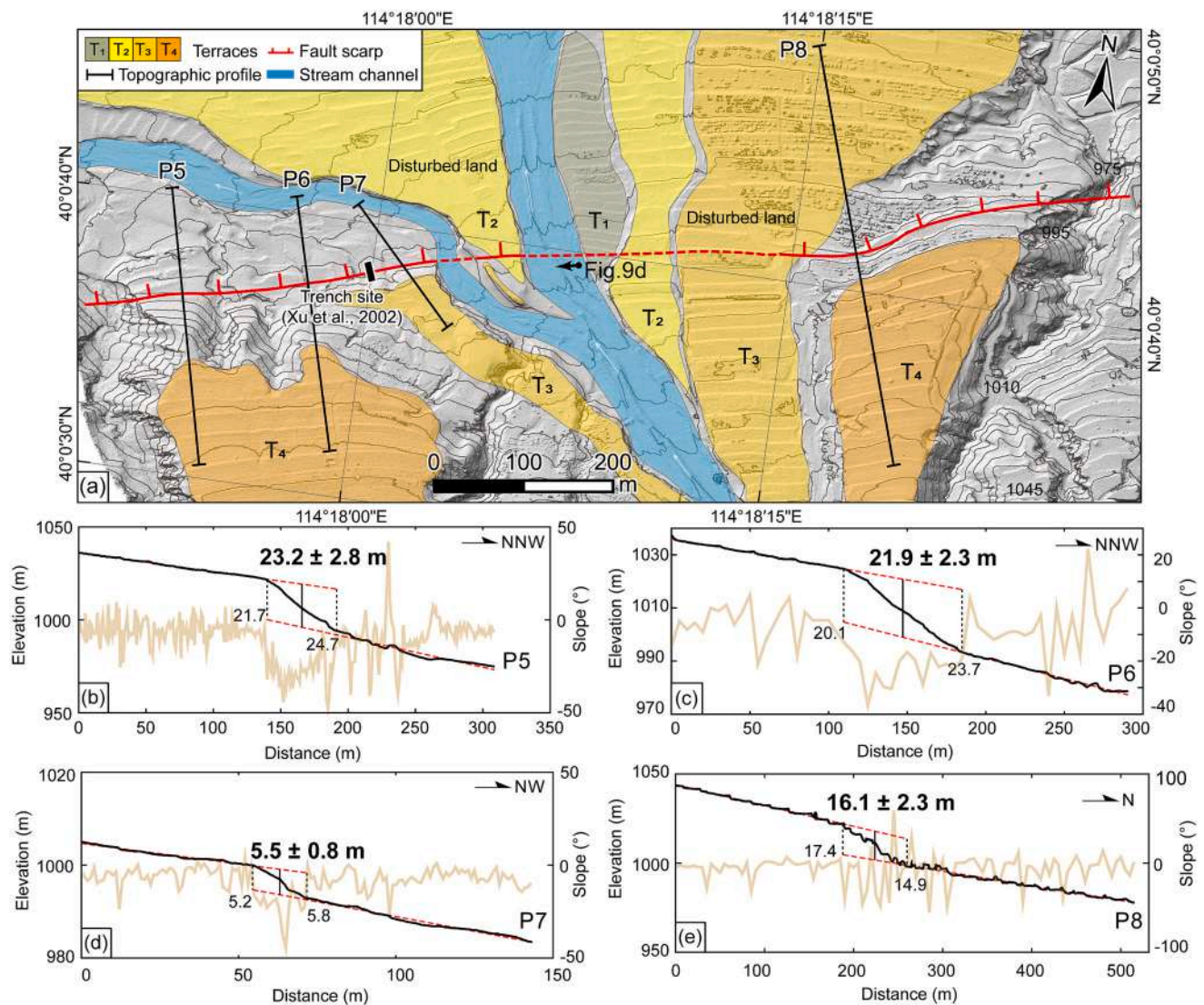


Fig. 11. Topographic map and profiles showing displaced geomorphic features in the vicinity of Shangzhuang village, with location shown in Fig. 1b. (a) Hillshade map overlain by 5 m-interval topographic contours showing terrace staircases, fault traces (red line), fault scarps (red teeth), and locations of topographic profiles. (b–e) Topographic profiles and slope profiles with locations are shown in Fig. 11a. (For interpretation of the references to colour in this figure legend, the reader is referred to the web version of this article.)

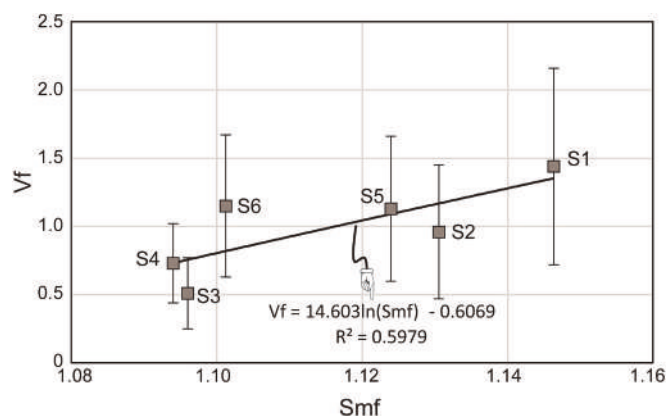


Fig. 12. Plot of S_{mf} versus V_f for the Liuleng Shan mountain front, showing relative tectonic activity. Data is referenced in Table S2.

conditions that are favorable for volcanism (Cunningham and Mann, 2007; Mathieu et al., 2011; Haddad et al., 2023). In fact, volcanoes of Quaternary age have developed in the central part of the NLSF within our identified releasing bend (Figs. 1b and 9b; Deng et al., 1994; Xu et al., 1996a). Magnetotelluric data reveal a high-conductivity anomaly in the middle crust below Yangyuan Basin (Fig. 5 in Zhang et al., 2016), which likely explains the source of magma. Deep seismic reflection data show that the NLSF is a crustal depth-scale fault (Zhang et al., 1998b). We infer that crustal extension within the releasing bend allowed magma to extrude to the surface along the fault zone of the NLSF. Zhang et al. (2016) argued that the Cenozoic magmatic intrusion process could influence seismicity in the northern SGS, including that of the 1989 earthquake swarm. Therefore, our proposed releasing bend fault model provides a mechanism for explaining volcanism and the source of earthquakes along the NLSF.

5.3. Implications for fault evolution and topography building

As established above, the kinematics of active faulting may differ from the fault's evaluation over time, primarily evidenced by HI values

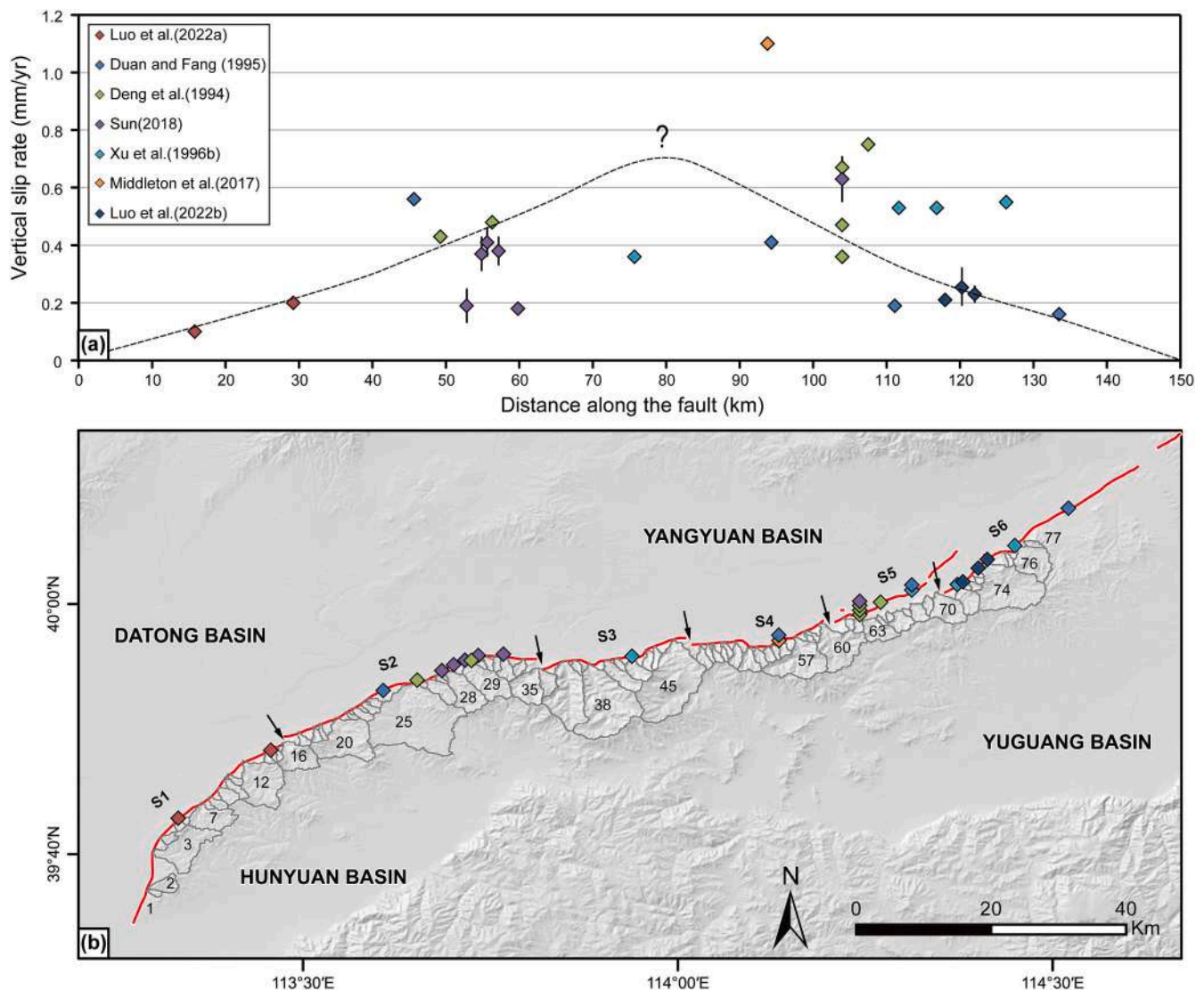


Fig. 13. Summary of vertical slip rates documented along the North Liuleng Shan Fault. Data referenced to Table S3. (a) Scatter plot showing published vertical slip rate data along the fault. (b) Hillshade map showing fault trace (red line), fault segmentation (black arrows), analyzed drainage basins (light gray polygons), and vertical slip rate study sites (squares). (For interpretation of the references to colour in this figure legend, the reader is referred to the web version of this article.)

that gradually increase from southwest to northeast (Fig. 5c). Regional basin evolution history sheds light on the development of the NLSF as well. The latest high-resolution magnetostratigraphic investigations of the DY-1 core in the Datong Basin show that the basal age of the sediments is approximately 7.0 Ma (Bi et al., 2022). As the southeastern boundary fault of the Datong Basin, the oblique right-lateral southwestern portion of the NLSF may have also reactivated around this time. We argue that the accumulation of right-lateral displacement along the southwestern portion of the NLSF eventually led to extension along the central and northeastern portions of the fault system, resulting in the pull-apart formation of the Yangyuan Basin in the early Pliocene and forming the ancient Nihewan Lake at about 4.2 Ma due to fault-controlled subsidence (Liu et al., 2018; Bi et al., 2022). Additionally, boreholes in the western part of the Yangyuan Basin contain Pliocene sediments, with sediment thickness of over 700 m, while early Pleistocene sediments in boreholes in the central and northeastern parts of the basin lie in direct and uncomfortable contact with the underlying bedrock, with sediment thickness of only 400–500 m (Xu et al., 2002). These geological observations, along with the increasing trend of HI values, indicate that the NLSF propagated from southwest to northeast over several million years.

Displacement generally decreases toward fault tips (Kim and Sanderson, 2005) and the largest magnitude displacement is typically located on the oldest and most mature sections of a fault, decreasing in the direction of long-term fault propagation (Manighetti et al., 2001, 2005; Perrin et al., 2016). The NLSF does not follow this trend. The central section of the fault zone uplifts most actively, evidenced by topographic swath profile and basin relief data (Figs. 3 and 5a). However, the central section is not the oldest section of the fault. Rather, the southwestern section of the NLSF initiated first, but due to the lateral-slip-dominated nature of the fault system, it accumulated minimal vertical displacement. The NLSF developed by the growth and connection of the southwestern and central-northeastern portions, which have different ages and activity patterns. This is responsible for the significant contrast in tectonic geomorphology of the southwestern and central-northeastern portions along the fault zone, as illustrated by this work and Cheng and Yang (1999).

The evolution pattern of the NLSF is consistent with the scissor-like opening model for the development of the basin and range structure of the northern SGS, in which basins spasmodically migrated and faults propagated from WSW to ENE (Xu and Ma, 1992; Xu et al., 1993). This model argues that the northern SGS evolved mainly by northeastward

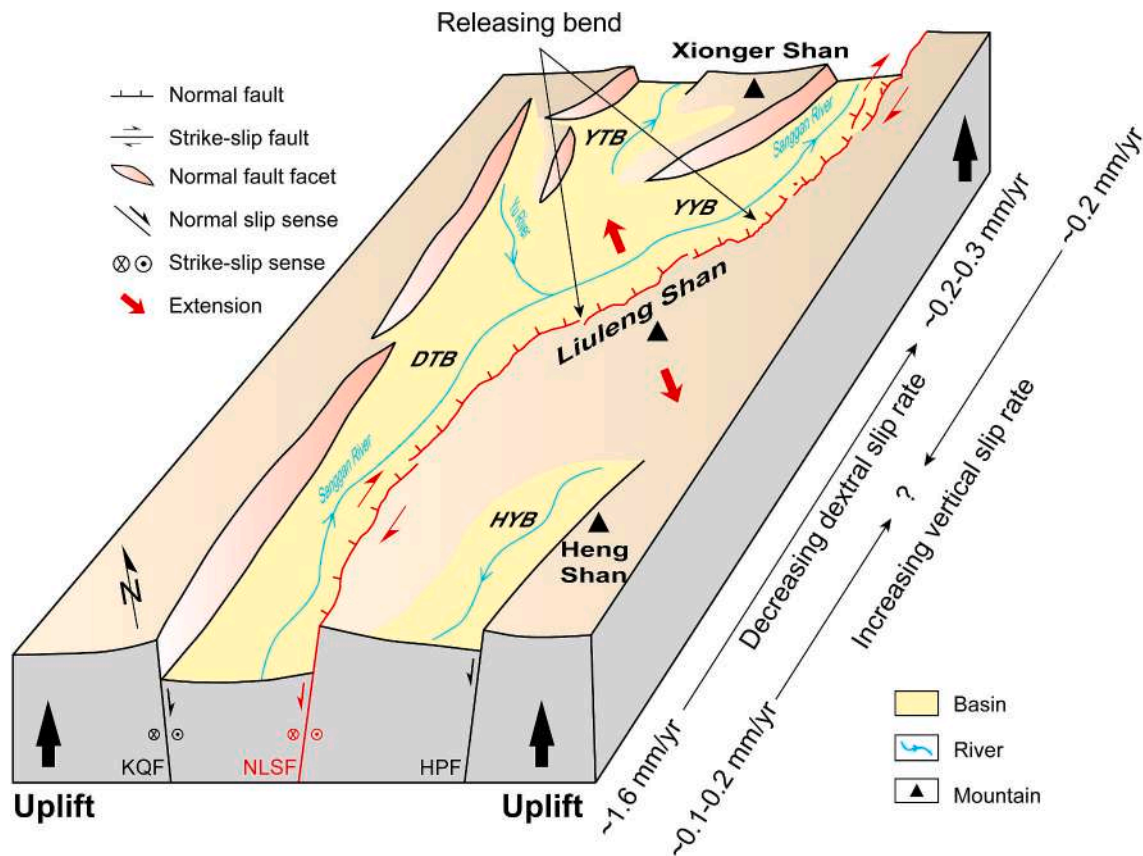


Fig. 14. Schematic model showing the deformation pattern of the North Liuleng Shan Fault. Note that the Z-shaped geometry and variations in fault kinematics along the fault strike will produce a releasing bend along the central portion of the fault. The right-lateral slip of the southwestern portion of the fault may be not completely absorbed and accommodated by crustal extension along the central portion and the remaining strain contributes to the right-lateral slip along the northeastern portion of the fault. Therefore, from the southwestern portion to the northeastern portion, the dextral slip rate decreases significantly, and the vertical slip rate increases from the northeast and southwest toward the center of the fault system. Abbreviations: YTB- Yanggao-Tianzhen Basin, DTB- Datong Basin, YYB- Yangyuan Basin, HYB- Hunyuan Basin; KQF- Kouquan Fault, NLSF- North Liuleng Shan Fault, HPF- Hengshan Piedmont Fault.

fault propagation from the northern end of the central, transtensional segment of the SGS (Fig. 1; Xu and Ma, 1992; Xu et al., 1993). In the early Pliocene, corrected to the late Miocene by subsequent studies (e.g., Shi et al., 2015), under a regional transtensional regime (NW-SE extension and NE-SW compression), NNE-SSW striking oblique right-lateral faults activated and north-south trending basin began to develop. Since the middle and late Pliocene, as a result of shear along the central transtensional segment of the SGS, the ENE-trending fault systems bounding sub-basins, including the Yanggao-Tianzhen, Yangyuan, Dingxiang, and Fanshi-Daixian basins, activated and resulted in the development of basin and range structures in the northern SGS (Xu and Ma, 1992). The Lingqiu and Yuguang basins, distant from the main shear zone of the SGS, began to develop in the early Pleistocene. In addition to basins developing more recently from southwest to northeast, block rotation amplitude and rate of vertical displacement of the range front faults and basin sediment thickness are also large in the southwest and gradually decrease toward the northeast (Xu and Deng, 1988; Xu et al., 1993). The NLSF conforms completely to these two characteristics. Our knowledge of the fault evolution history of the NLSF is of great significance to the improvement of the origin of the basin-and-range geomorphology in the northern SGS.

6. Conclusion

In this work, we evaluate the distribution of relative uplift rates along the NLSF using geomorphic indices including slope, mountain front sinuosity (S_{mf}), hypsometric integral (HI) and curves, valley floor width-to-height ratio (V_f), asymmetry factor (A_f), basin elongation ratio

(R_e), and normalized steepness indices (k_{sn}). The results show that the central portion of the fault has experienced the highest relative uplift rates, followed by the northeastern portion and finally the southwestern portion. This distribution appears to be closely related to the along-strike variations in fault geometry and kinematics. The Z-shaped NLSF consists of the NE-striking, right-stepping, en-echelon-arranged southwestern and northeastern portions and the EW-striking central section. The central portion of the fault is dominated by normal faulting, while the southwestern and northeastern portions of the fault are characterized by oblique right-lateral slip. We interpret the central portion of the NLSF as a “releasing bend”. The higher right-lateral slip along the southwestern portion (~ 1.6 mm/yr) is not completely absorbed by the crustal extension of the central portion and is partially transferred to the slip along the northeastern portion (~ 0.2 – 0.3 mm/yr). This is likely the reason for the significant reduction of the right-lateral slip rate of the northeastern portion. Additionally, the increasing trend of HI values and the changing of hypsometric curve shapes from southwest to northeast suggest that the NLSF developed from southwest to northeast. This interpretation is supported by the regional basin evolution history: the Datong Basin commenced in the late Miocene, while the Yangyuan Basin was initiated in the Pliocene. Further, the Yangyuan basin depth decreases eastward, and the basal sediment age becomes younger from west to east. Therefore, we favor the interpretation that the southwestern portion of the fault that bounds the southeastern margin of the Datong Basin initiated earlier, and the central and northeastern portions of the fault formed later as extensional structures at the northeastern termini of the southwestern portion of the fault zone. We recognize the present NLSF as a result of the connection and growth of fault segments

of different ages and fault kinematics. Our results not only contribute to the understanding of the tectonic deformation pattern and evolutionary history of the NLSF but also to regional volcanic and seismic hazards and a wider understanding of the development of the northern SGS. Further research is needed to quantify the vertical slip rate along the central portion of the fault and to estimate the timing of initiation along the fault system.

Declaration of competing interest

The authors declare that they have no known competing financial interests or personal relationships that could have appeared to influence the work reported in this paper.

Data availability

The data that has been used is confidential.

Acknowledgment

The MERIT DEM used to extract geomorphic indices and UAV survey data are archived in Mendeley Data at <https://data.mendeley.com/datasets/xmxxgvwrdg/1>. This work is financed by the National Natural Science Foundation of China (41971002, 42072250, and U2039201) and the National Key Research and Development Program of China (2017YFC1500100). We acknowledge support from the China Scholarship Council (CSC) during a visit of Quanxing Luo (202106010138) to the University of Toronto. We thank the two anonymous referees for their helpful comments which greatly improved our manuscript. Dr. Achim A. Beylich (Editor-in-Chief,) and Prof. Efthimios Karymbalis (Executive Guest Editor) are appreciated for editing the manuscript.

Appendix A. Supplementary data

Supplementary data to this article can be found online at <https://doi.org/10.1016/j.geomorph.2023.108862>.

References

- Ai, S.X., Zheng, Y., Riaz, M.S., et al., 2019. Seismic evidence on different rifting mechanisms in southern and northern segments of the Fenhe-Weihe Rift zone. *Journal of Geophysical Research: Solid Earth* 124 (1), 609–630. <https://doi.org/10.1029/2018JB016476>.
- Barbour, G.B., 1924. Preliminary observation in Kalgan area. *Bulletin of the Geological Society of China* 3, 167–168. <https://doi.org/10.1111/j.1755-6724.1924.mp3002009.x>.
- Bi, Y.P., Pang, E.C., Sun, Y.S., et al., 2022. Magnetostratigraphy of the fluvio-lacustrine sequence of core DY-1 in the Datong Basin and its implications for the evolution of the Shanxi Rift System in northern China. *Palaeogeogr. Palaeoclimatol. Palaeoecol.* 599, 111063 <https://doi.org/10.1016/j.palaeo.2022.111063>.
- Bucci, M.G., Schoenbohm, L.M., 2022. Tectono-Geomorphic Analysis in Low Relief, Low Tectonic activity areas: Case Study of the Temiskaming Region in the Western Quebec Seismic Zone (WQSZ), Eastern Canada. *Remote Sensing* 14 (15), 3587. <https://doi.org/10.3390/rs14153587>.
- Bull, W.B., McFadden, L.D., 1977. Tectonic geomorphology North and South of the Garlock Fault, California. In: Doehring, D.O. (Ed.), *Geomorphology in Arid Regions: A Proceedings Volume of the 8th Annual Geomorphology Symposium*. State University of New York, Binghamton, 23–24 September 1977, p. 115–138.
- Cheng, S.P., Yang, G.Z., 1999. Segmented variations in tectonic geomorphology of Datong-yangyuan fault zone, NW Beijing, China. *Journal of the Balkan Geophysical Society* 2 (2), 46–62.
- Cheng, Y.L., He, C.Q., Rao, G., et al., 2018. Geomorphological and structural characterization of the southern Weihe Graben, Central China: Implications for fault segmentation. *Tectonophysics* 722, 11–24. <https://doi.org/10.1016/j.tecto.2017.10.024>.
- Clinkscales, C., Kapp, P., Wang, H.Q., 2020. Exhumation history of the north-Central Shanxi Rift, North China, revealed by low-temperature thermochronology. *Earth Planet. Sci. Lett.* 536, 116146 <https://doi.org/10.1016/j.epsl.2020.116146>.
- Clinkscales, C., Kapp, P., Thomson, S., et al., 2021. Regional exhumation and tectonic history of the Shanxi rift and Taihangshan, North China. *Tectonics* 40 (3), e2020TC006416. <https://doi.org/10.1029/2020TC006416>.
- Cunningham, W.D., Mann, P., 2007. Tectonics of strike-slip restraining and releasing bends. *Geol. Soc. Lond., Spec. Publ.* 290 (1), 1. <https://doi.org/10.1144/SP290.1>.
- Deng, C., Zhu, R., Zhang, R., Ao, H., Pan, Y., 2008. Timing of the Nihewan formation and faunas. *Quat. Res.* 69 (1), 77–90. <https://doi.org/10.1016/j.yqres.2007.10.006>.
- Deng, Q.D., Xu, X.W., 1995. Study on active faults and segmentation of Shanxi Graben System (in Chinese). *Research on Modern Crustal Movement* 6, 225–241.
- Deng, Q.D., Nobuyuki, Y., Xu, X.W., et al., 1994. Study on the late quaternary kinematics of the northern piedmont fault of the Liuleng Mountain (in Chinese). *Seismology and Geology* 16, 339–343.
- Deng, Q.D., Cheng, S.P., Min, W., Yang, G.Z., Ren, D.W., 1999. Discussion on Cenozoic tectonics and dynamics of Ordos block (in Chinese). *J. Geom.* 5, 13–21.
- DiBiase, R.A., Whipple, K.X., Heimsath, A.M., Ouimet, W.B., 2010. Landscape form and millennial erosion rates in the San Gabriel Mountains, CA. *Earth Planet. Sci. Lett.* 289, 134–144. <https://doi.org/10.1016/j.epsl.2009.10.036>.
- Dou, L.T., Yao, H.J., Fang, L.H., et al., 2021. High-resolution crustal velocity structure in the Shanxi rift zone and its tectonic implications. *Sci. China Earth Sci.* 64 (5), 728–743.
- Duan, R.T., Fang, Z.J., 1995. Neotectonic characteristics of the northern piedmont fault of the Liuleng Mountain (in Chinese). *Seismology and Geology* 17, 207–213.
- El Hamdouni, R., Irigaray, C., Fernández, T., et al., 2008. Assessment of relative active tectonics, southwest border of the Sierra Nevada (southern Spain). *Geomorphology* 96, 150–173. <https://doi.org/10.1016/j.geomorph.2007.08.004>.
- Flint, J.J., 1974. Stream gradient as a function of order, magnitude, and discharge. *Water Resour. Res.* 10, 969e973.
- Forte, A.M., Whipple, K.X., 2019. Short Communication: the Topographic Analysis Kit (TAK) for TopoToolbox. *Earth Surface Dynamics* 7, 87–95. <https://doi.org/10.5194/esurf-7-87-2019>.
- Gusti, U., Peace, A., Rimando, J., 2023. Tectonic geomorphology of the Ottawa-Bonnechere Graben, Eastern Canada: implications for regional uplift and intraplate seismicity. *Can. J. Earth Sci.* <https://doi.org/10.1139/cjes-2022-0137>.
- Hack, J.T., 1957. *Studies of Longitudinal Stream Profiles in Virginia and Maryland*. U.S. Geological Survey Professional Paper 294-B, p. 97.
- Haddad, A., Chiarabba, C., Lazar, M., et al., 2023. Rifting-driven magmatism along the Dead Sea continental transform Fault. *Geophys. Res. Lett.* 50, e2022GL099964 <https://doi.org/10.1029/2022GL099964>.
- Hao, M., Wang, Q.L., Zhang, P.Z., Li, Z.J., Li, Y.H., Zhuang, W.Q., 2021. “Frame Wobbling” causing crustal deformation around the Ordos Block. *Geophys. Res. Lett.* 48, e2020GL091008 <https://doi.org/10.1029/2020GL091008>.
- Hare, P.H., Gardner, T.W., 1985. Geomorphic indicators of vertical neotectonism along converging plate margins, Nicoya Peninsula, Costa Rica. In: Morisawa, M., Hack, J.T. (Eds.), *Tectonic Geomorphology*. Allen and Unwin, Boston, pp. 75–104.
- Harkins, N., Kirby, E., Heimsath, A., Robinson, R., Reiser, U., 2007. Transient fluvial incision in the headwaters of the Yellow River, northeastern Tibet, China. *Journal of Geophysical Research: Earth Surface* 112, F03S04.
- Johnson, K., Nissen, E., Saripalli, S., et al., 2014. Rapid mapping of ultrafine fault zone topography with structure from motion. *Geosphere* 10 (5), 969–986. <https://doi.org/10.1130/GES01017.1>.
- Kim, Young-Seog, Sanderson, D.J., 2005. The relationship between displacement and length of faults: a review. *Earth Sci. Rev.* 68, 317–334. <https://doi.org/10.1016/j.earscirev.2004.06.003>.
- King, G., Nabelek, J., 1985. Role of fault bends in the initiation and termination of earthquake rupture. *Science* 228 (4702), 984–987. <https://doi.org/10.1126/science.228.4702.984>.
- Kirby, E., Whipple, K.X., 2001. Quantifying differential rock-uplift rates via stream profile analysis. *Geology* 29 (5), 415–418.
- Kirby, E., Whipple, K.X., 2012. Expression of active tectonics in erosional landscapes. *J. Struct. Geol.* 44, 54–75. <https://doi.org/10.1016/j.jsg.2012.07.009>.
- Kirby, E., Whipple, K.X., Tang, W.Q., Chen, Z.L., 2003. Distribution of active rock uplift along the eastern margin of the Tibetan Plateau: Inferences from bedrock channel longitudinal profiles. *J. Geophys. Res.* 108 (B4), 2217. <https://doi.org/10.1029/2001JB000861>.
- Krystopowicz, N.J., Schoenbohm, L.M., Rimando, J., et al., 2019. Tectonic geomorphology and Plio-Quaternary structural evolution of the Tuzgözü fault zone, Turkey: Implications for deformation in the interior of the Central Anatolian Plateau. *Geosphere* 16 (5), 1107–1124. <https://doi.org/10.1130/GES02175.1>.
- Li, C.Y., Wang, X.C., He, C.Z., Kong, Z., Li, X., 2017. National 1:200 000 digital geological map (open edition) spatial database (V1). In: Development Research Center of China Geological Survey; China Geological Survey, 1957. China, National Geological Archive of.
- Li, X.N., Pierce, I.K.D., Ai, M., et al., 2022. Active tectonics and landform evolution in the Longxian-Baoji Fault Zone, Northeast Tibet, China, determined using combined ridge and stream profiles. *Geomorphology* 410, 108279. <https://doi.org/10.1016/j.geomorph.2022.108279>.
- Li, Y.L., Yang, J.C., Xia, Z.K., et al., 1998. Tectonic geomorphology in the Shanxi Graben System, northern China. *Geomorphology* 23, 77–89.
- Liu, K., Song, C.Q., Ke, L.H., et al., 2019. Global open-access DEM performances in Earth's most rugged region High Mountain Asia: a multi-level assessment. *Geomorphology* 338, 16–26. <https://doi.org/10.1016/j.geomorph.2019.04.012>.
- Liu, P., Yue, F., Liu, J.Q., et al., 2018. Magnetostratigraphic dating of the Shixia red sediments and implications for formation of Nihewan paleo-lake, North China. *Quat. Sci. Rev.* 193, p.118–128. doi:<https://doi.org/10.1016/j.quascirev.2018.06.013>.
- Luo, Q., Li, Y., Schoenbohm, L., Rimando, J., et al., 2022b. Direct evidence for dextral shearing in the Shanxi Graben System: Geologic and geomorphologic constraints from the North Liulengshan Fault. *Tectonics* 41, e2022TC007490. <https://doi.org/10.1029/2022TC007490>.
- Luo, Q.X., Li, C.Y., Li, X.N., et al., 2021. Slip distribution and footwall topography of the Yanggao-Tianzhen Fault (northern Shanxi Graben): Implications for the along-strike

- variations in fault activity and regional deformation. *Tectonics* 40, e2020TC006593. <https://doi.org/10.1029/2020TC006593>.
- Luo, Q.X., Li, Y.L., Hu, X., Guo, A.L., Liu, Q.R., Jiang, S.R., 2022a. Constrains on the late quaternary dextral strike-slip rate of the western segment of the North Liulengshan fault in the northern Shanxi Graben system (in Chinese). *Quaternary Sciences* 42. <https://doi.org/10.11928/j.issn.1001-7410.2022.03.08>.
- Luo, Q.X., Li, C.Y., Ren, G.X., et al., 2023. The 1673 Tianzhen earthquake and rupture behavior of the Yanggao-Tianzhen Fault in the northern Shanxi Graben, China. *Tectonics* 42, e2022TC007582. <https://doi.org/10.1029/2022TC007582>.
- Lv, S.H., Li, Y.L., Wang, Y.R., et al., 2014. The Holocene paleoseismicity of the North Zhongtiaoshan Faults in Shanxi Province, China. *Tectonophysics* 623, 67–82. <https://doi.org/10.1016/j.tecto.2014.03.019>.
- Manighetti, I., King, G.C.P., Gaudemer, Y., Scholz, C.H., Doubre, C., 2001. Slip accumulation and lateral propagation of active normal faults in Afar. *J. Geophys. Res.* 106 (B7), 13,667–13,696. <https://doi.org/10.1029/2000JB900471>.
- Manighetti, I., Campillo, M., Sammis, C., Mai, P.M., King, G., 2005. Evidence for self-similar, triangular slip distributions on earthquakes: Implications for earthquake and fault mechanics. *J. Geophys. Res.* 110, B05302. <https://doi.org/10.1029/2004JB003174>.
- Mathieu, L., van Wyk de Vries, B., Pilato, M., et al., 2011. The interaction between volcanoes and strike-slip, transtensional and transpressional fault zones: Analogue models and natural examples. *J. Struct. Geol.* <https://doi.org/10.1016/j.jsg.2011.03.003>.
- Middleton, T.A., Elliott, J.R., Rhodes, E.J., Sherlock, S., Walker, R.T., Wang, W.T., Yu, J. X., Zhou, Y., 2017. Extension rates across the northern Shanxi Grabens, China, from Quaternary geology, seismicity, and geodesy. *Geophys. J. Int.* <https://doi.org/10.1093/gji/ggx031>.
- Mitchell, N.A., Yanites, B.J., 2019. Spatially variable increase in rock uplift in the northern U.S. Cordillera recorded in the distribution of river knickpoints and incision depths. *Journal of Geophysical Research: Earth Surface* 124, 1238–1260. <https://doi.org/10.1029/2018JF004880>.
- Molin, P., Pazzaglia, F.J., Dramis, F., 2004. Geomorphic expression of active tectonics in a rapidly-deforming forearc, Sila massif, Calabria, southern Italy. *Am. J. Sci.* 304 (7), 559–589. <https://doi.org/10.2475/ajs.304.7.559>.
- Ntkos, D., Lykoudi, E., Rondoyanni, T., 2016. Geomorphic analysis in areas of low-rate neotectonic deformation: South Epirus (Greece) as a case study. *Geomorphology* 263, 156–169. <https://doi.org/10.1016/j.geomorph.2016.04.005>.
- Pardo, C.D., Smith-Konte, B.R., Serpa, L.F., et al., 2012. Interseismic deformation and geologic evolution of the Death Valley Fault Zone. *Journal of Geophysical Research: Solid Earth*. <https://doi.org/10.1029/2011JB008552>.
- Pérez-Peña, J.V., Azor, A., Azanón, J.M., et al., 2010. Active tectonics in the Sierra Nevada (Betic Cordillera, SE Spain): Insights from geomorphic indexes and drainage pattern analysis. *Geomorphology* 119, 74–87. <https://doi.org/10.1016/j.geomorph.2010.02.020>.
- Pérez-Peña, J.V., Al-Awaddeh, M., Azanón, J.M., et al., 2017. SwathProfiler and NProfiler: two new ArcGIS Add-ins for the automatic extraction of swath and normalized river profiles. *Comput. Geosci.* 104, 135–150. <https://doi.org/10.1016/j.cageo.2016.08.008>.
- Perrin, C., Manighetti, I., Ampuero, J.P., et al., 2016. Location of largest earthquake slip and fast rupture controlled by along-strike change in fault structural maturity due to fault growth. *Journal of Geophysical Research: Solid Earth* 121, 3666–3685. <https://doi.org/10.1002/2015JB012671>.
- Rimando, J.M., Schoenbohm, L.M., 2020. Regional relative tectonic activity of structures in the Pampean flat slab segment of Argentina from 30 to 32° S. *Geomorphology* 350. <https://doi.org/10.1016/j.geomorph.2019.106908>.
- Rockwell, T.K., Keller, E.A., Johnson, D.L., 1985. Tectonic geomorphology of alluvial fans and mountain fronts near Ventura, California. In: Morisawa, M. (Ed.), *Tectonic Geomorphology*. Allen and Unwin Publishers, Boston, MA, pp. 183–207. *Proceedings of the 15th Annual Geomorphology Symposium*.
- Saber, R., Caglayan, A., Isik, V., 2018. Relative tectonic activity assessment and kinematic analysis of the North Bozghush fault Zone, NW Iran. *J. Asian Earth Sci.* 164, 219–236. <https://doi.org/10.1016/j.jseas.2018.06.023>.
- Schumm, S.A., 1956. Evolution of drainage systems and slopes in badlands at PerthAmboy, New Jersey. *Bull. Geol. Soc. Am.* 67 (5), 597–646. [https://doi.org/10.1130/0016-7606\(1956\)67\[597:EODSAS\]2.0.CO;2](https://doi.org/10.1130/0016-7606(1956)67[597:EODSAS]2.0.CO;2).
- Schwanghart, W., Nikolaus, J.K., 2010. TopoToolbox: a set of Matlab functions for topographic analysis. *Environ. Model. Softw.* 25 (6), 770–781. ISSN 13648152. <https://doi.org/10.1016/j.envsoft.2009.12.002>.
- Schwanghart, W., Scherler, D., 2014. Short Communication: TopoToolbox 2 - MATLAB based software for topographic analysis and modeling in Earth surface sciences. *Earth Surface Dynamics* 2, 1–7. <https://doi.org/10.5194/esurf-2-1-2014>.
- Selby, M.J., 1980. A rock strength classification for geomorphic purposes: with tests from Antarctica and New Zealand. *Z. Geomorphol.* 24, 31–51. <https://doi.org/10.1127/zfg/24/1984/31>.
- Shi, W., Cen, M., Chen, L., Wang, Y.C., Chen, X.Q., Li, J.Y., Chen, P., 2015. Evolution of the late Cenozoic tectonic stress regime in the Shanxi Rift, central North China Plate inferred from new fault kinematic analysis. *J. Asian Earth Sci.* 114, 54–72. <https://doi.org/10.1016/j.jseas.2015.04.044>.
- Shi, W., Dong, S.W., Hu, J.M., 2020a. Neotectonics around the Ordos Block, North China: a review and new insights. *Earth Sci. Rev.* 200, 102969. <https://doi.org/10.1016/j.earscirev.2019.102969>.
- Shi, X.H., Yang, Z., Dong, Y.P., et al., 2020b. Geomorphic indices and longitudinal profile of the Daba Shan, northeastern Sichuan Basin: evidence for the late Cenozoic eastward growth of the Tibetan Plateau. *Geomorphology* 353, 107031. <https://doi.org/10.1016/j.geomorph.2020.107031>.
- Silva, P.G., Goy, J.L., Zazo, C., et al., 2003. Fault-generated mountain fronts in Southeast Spain: geomorphologic assessment of tectonic and seismic activity. *Geomorphology* 50, 203–225. [https://doi.org/10.1016/S0169-555X\(02\)00215-5](https://doi.org/10.1016/S0169-555X(02)00215-5).
- Small, E.E., Anderson, R.S., 1998. Pleistocene relief production in Laramide mountain ranges, western United States. *Geology* 26, 123–126. [https://doi.org/10.1130/0091-7613\(1998\)026<0123:PRPILM>2.3.CO;2](https://doi.org/10.1130/0091-7613(1998)026<0123:PRPILM>2.3.CO;2).
- Strahler, A.N., 1952. Hypsometric (area-altitude) analysis of erosional topography. *Bull. Geol. Soc. Am.* 63 (11), 1117–1142.
- Strahler, A.N., 1964. Quantitative geomorphology of drainage basins and channel networks. In: Chow, V.T. (Ed.), *Handbook of Applied Hydrology*. Mc Graw-Hill, New York, pp. 4.40–4.74.
- Su, P., He, H.L., Tan, X.B., et al., 2021. Initiation and evolution of the Shanxi rift system in North China: evidence from low-temperature thermochronology in a Plate reconstruction framework. *Tectonics* 40 (3), e2020TC006298. <https://doi.org/10.1029/2020TC006298>.
- Sun, W., 2018. Late Quaternary Activity of Liuleng Mountain North Fault (in Chinese). Master's Thesis submitted to Institute of Geology, China Earthquake Administration. Retrieved from <https://chn.oversea.cnki.net/kcms/detail/detail.aspx?FileName=1018300069.nh%26DbName=CMFD2019>.
- Sun, W., He, H.L., Shi, F., et al., 2023. Late-Quaternary paleoearthquakes along the Liulengshan Fault on the northern Shanxi Rift system. *Front. Earth Sci.* <https://doi.org/10.3389/feart.2022.954335>.
- Telbisz, T., Kovács, G., Székely, B., et al., 2013. Topographic swath profile analysis: a generalization and sensitivity evaluation of a digital terrain analysis tool. *Z. Geomorphol.* 57 (4), 485–513. <https://doi.org/10.1127/0372-8854/2013/0110>.
- Thompson Jobe, J.A., Gold, R.D., Briggs, R.W., et al., 2020. Evidence for late Quaternary deformation along Crowleys Ridge, New Madrid seismic zone. *Tectonics* 39, e2019TC005746. <https://doi.org/10.1029/2019TC005746>.
- Uuemaa, E., Ahi, S., Montibeller, B., et al., 2020. Vertical accuracy of freely available global digital elevation models (ASTER, AW3D30, MERIT, TanDEM-X, SRTM, and NASADEM). *Remote Sens.* 12, 3482. <https://doi.org/10.3390/rs12213482>.
- Wang, H., Liu, M., Ye, J.Y., et al., 2017. Strain partitioning and stress perturbation around stepovers and bends of strike-slip faults: Numerical results. *Tectonophysics* 721, 211–226. <https://doi.org/10.1016/j.tecto.2017.10.001>.
- Wang, M., Shen, Z.K., 2020. Present-day crustal deformation of continental China derived from GPS and its tectonic implications. *Journal of Geophysical Research: Solid Earth* 125, e2019JB018774. <https://doi.org/10.1029/2019JB018774>.
- Whipple, K., Tucker, G., 2002. Implications of sediment-flux dependent river incision models for landscape evolution. *J. Geophys. Res.* 107. <https://doi.org/10.1029/2000JB000044>.
- Wobus, C., Whipple, K.X., Kirby, E., et al., 2006. Tectonics from topography: Procedures, promise, and pitfalls. In: Willett, S.D., Hovius, N., Brandon, M.T., Fisher, D.M. (Eds.), *Tectonics, Climate, and Landscape Evolution: Geological Society of America Special Paper 398*. Penrose Conference Series, pp. 55–74. [https://doi.org/10.1130/2006.2398\(04](https://doi.org/10.1130/2006.2398(04).
- Wobus, C.W., Hodges, K.V., Whipple, K.X., 2003. Has focused denudation sustained active thrusting at the Himalayan topographic front? *Geology* 31 (10), 861–864. <https://doi.org/10.1130/G19730.1>.
- Xu, X.W., Deng, Q.D., 1988. The basin-range structure in the tensile area at the northern part of Shanxi Province and its mechanism of formation (in Chinese). *Earthquake Research in China* 4 (2), 19–27.
- Xu, X.W., Ma, X.Y., 1992. Geodynamics of the Shanxi Rift system, China. *Tectonophysics* 208, 325–340.
- Xu, X.W., Ma, X.Y., Deng, Q.D., 1993. Neotectonic activity along the Shanxi rift system, China. *Tectonophysics* 219, 305–325.
- Xu, X.W., Nobuyuki, Y., Suzuki, Y., et al., 1996a. Geomorphic study on late Quaternary irregular faulting along the northern piedmont of Liulengshan range, Shanxi Province, China (in Chinese). *Seismology and Geology* 18, 169–181.
- Xu, X.W., Ma, X.Y., Deng, Q.D., et al., 1996b. Neotectonics, Paleoseismology and Ground Fissures of the Shanxi (Fenwei) Rift System. China. (In 30th international geological congress field trip guide T314).
- Xu, X.W., Wu, W.M., Zhang, X.K., et al., 2002. Recent Tectonic Changes and Earthquakes in the Crust of the Capital Area (in Chinese). Science Publishing House.
- Xu, X.W., Wu, X.Y., Yu, G.H., et al., 2017. Seismo-geological signatures for identifying M_{7.0} earthquake risk areas and their preliminary application in mainland China (in Chinese). *Seismology and Geology* 39 (2), 219–275. <https://doi.org/10.3969/j.issn.0253-4967.2017.02.001>.
- Yan, D.D., Lv, S.H., Zhao, H.Z., et al., 2011. Geomorphic analysis and its implication to Neotectonics in middle of northern front of Liulengshan Mountain, Northern Shanxi. *Scientia Geographica Sinica* 31 (2), 244–250.
- Yazıcı, M., Zabcı, C., Sançar, T., Natalin, B.A., 2018. The role of intraplate strike-slip faults in shaping the surrounding morphology: the Ovacık Fault (eastern Turkey) as a case study. *Geomorphology*. <https://doi.org/10.1016/j.geomorph.2018.08.022>.
- Yıldırım, C., 2014. Relative tectonic activity assessment of the Tuz Gölü Fault Zone; Central Anatolia, Turkey. *Tectonophysics* 630, 183–192. <https://doi.org/10.1016/j.tecto.2014.05.023>.
- Yin, G.M., Xu, X.W., Sun, Y.J., et al., 1997. Study on the paleoearthquake chronology of the northern piedmont fault of the Liulengshan range of Yangyuan, Hebei Province, China (in Chinese). *Earthquake Research in China* 13, 18–26.
- Zhang, C.K., Zhang, X.K., Gai, Y.J., et al., 1998b. The crust-mantle velocity structure and deep tectonics in the Datong-Yanggao seismic region and its adjacent area (in Chinese). *Seismology and Geology* 20 (4), 391–398.
- Zhang, H.P., Zhang, P.Z., Kirby, E., et al., 2011. Along-strike topographic variation of the Longmen Shan and its significance for landscape evolution along the eastern Tibetan Plateau. *J. Asian Earth Sci.* 40, 855–864. <https://doi.org/10.1016/j.jseas.2010.05.015>.

- Zhang, H.Q., Huang, Q.H., Zhao, G.Z., et al., 2016. Three-dimensional conductivity model of crust and uppermost mantle at the northern Trans North China Orogen: evidence for a mantle source of Datong volcanoes. *Earth Planet. Sci. Lett.* 453, 182–192. <https://doi.org/10.1016/j.epsl.2016.08.025>.
- Zhang, Y.Q., Mercier, J.L., Vergely, P., 1998a. Extension in the graben systems around the Ordos (China), and its contribution to the extrusion tectonics of South China with respect to Gobi-Mongolia. *Tectonophysics* 285 (1–2), 41–75. [https://doi.org/10.1016/s0040-1951\(97\)00170-4](https://doi.org/10.1016/s0040-1951(97)00170-4).
- Zhao, B., Zhang, C.H., Wang, D.Z., et al., 2017. Contemporary kinematics of the Ordos block, North China and its adjacent rift systems constrained by dense GPS observations. *J. Asian Earth Sci.* 135, 257–267. <https://doi.org/10.1016/j.jseaes.2016.12.045>.
- Zhu, R.X., Hoffman, K.A., Potts, R., et al., 2001. Earliest presence of humans in Northeast Asia. *Nature* 413, 413–417. <https://doi.org/10.1038/35096551>.
- Zhu, R.X., Potts, R., Xie, F., et al., 2004. New evidence on the earliest human presence at high northern latitudes in Northeast Asia. *Nature* 431, 559–562. <https://doi.org/10.1038/nature02829>.
- Zhuo, Y.Q., Guo, Y.S., Bornyakov, S.A., et al., 2019. A test of the oblique-rifting model for transfer zone deformation in the northern Fen-Wei Rift: Implications from the 1989 M 6.1 Datong-Yanggao earthquake swarm. *Geodynamics & Tectonophysics* 10 (1), 43–51. <https://doi.org/10.5800/GT-2019-10-1-0403>.